Journal of Power Sources 208 (2012) 96–119

Contents lists available at SciVerse ScienceDirect

Journal of Power Sources

journal homepage: www.elsevier.com/locate/jpowsour

Review

Support materials for PEMFC and DMFC electrocatalysts—A review

Surbhi Sharma*, Bruno G. Pollet

PEM Fuel Cell Research Group, Centre for Hydrogen and Fuel Cell Research, College of Engineering and Physical Sciences, The University of Birmingham, Edgbaston Road, Birmingham, B15 2TT, UK

ARTICLE INFO

Article history:
Received 22 October 2011
Received in revised form 31 January 2012
Accepted 5 February 2012
Available online 1 March 2012

Keywords:
Direct methanol fuel cells (DMFC)
Polymer electrolyte membrane fuel cells (PEMFC)
Electrocatalyst support
Hybrid support
Review

ABSTRACT

Polymer electrolyte membrane fuel cells (PEMFC) and direct methanol fuel cells (DMFC) have found a wide variety of commercial applications. Their performance is essentially governed by the electrocatalyst support materials as they strongly influence the electrocatalyst performance, durability and efficiency. It is well known that carbonaceous support materials suffer from carbon corrosion (oxidation) especially at high potentials over time and thus alternative low-cost, high-performing and non-corrosive electrocatalyst support materials are urgently required. This review highlights the performance and issues associated with a variety of carbon based materials such as carbon nanotubes (CNT), carbon nanofibers (CNF), mesoporous carbon and graphene as well as non-carbonaceous based materials, e.g. titania, indium oxides, alumina, silica and tungsten oxide and carbide, ceria, zirconia nanostructures and conducting polymers catalyst support materials. Comparisons and advantages and disadvantages of the various supports are clearly described in this review.

Contents

* Corresponding author. Tel.: +44 121 414 5081; fax: +44 121 414 5324.
E-mail address: s.sharma.1@bham.ac.uk (S. Sharma).

0378-7753/$ – see front matter © 2012 Elsevier B.V. All rights reserved.
doi:10.1016/j.jpowsour.2012.02.011

1. Introduction

The world's ever increasing energy requirement, continuous and rapid depletion of fossil fuels along with alarming increase in the concentration of greenhouse gases have directed large scale research into the development of alternative and 'greener' energy sources. Consequently, fuel cells which have very low or even zero emission of harmful greenhouse gases (e.g. CO_2, NO_x, SO_x, etc.), have generated a lot of interest amongst the scientific and engineering communities [1–5]. Today, fuel cells are widely considered to be efficient and non-polluting power sources offering much higher energy densities and energy efficiencies compared to other current/conventional systems. A fuel cell is an 'electrochemical' device that converts the chemical energy of a fuel (e.g. hydrogen, methanol, etc.) and an oxidant (air or pure oxygen) in the presence of a catalyst into electricity, heat and water. Currently, there are six main types of fuel cells, namely [6–11]: (i) proton exchange membrane fuel cell (PEMFC) including direct methanol fuel cell (DMFC), (ii) alkaline fuel cell (AFC), (iii) phosphoric acid fuel cell (PAFC), (iv) molten carbonate fuel cell (MCFC), (v) solid oxide fuel cell (SOFC) and (vi) microbial fuel cell (MFC). PEMFC, DMFC, AFC, PAFC, and MFC operate at low temperatures [50–200 °C] and MCFC and SOFC at high temperatures [650–1000 °C].

The main objective in fuel cell technologies is to develop low-cost, high-performance and durable materials. However, current fuel cell systems have high intrinsic costs and fairly poor durability. Several avenues have been explored with the aim to reduce the cost and increase the performance of a fuel cell. These can broadly be listed as [6–11]:

(i) Reducing the electrocatalyst loading in fuel cell electrodes.
(ii) Developing novel nano-structured thin-film Pt (e.g. 3M's nano structured thin film (NSTF) electrode).
(iii) Decreasing the electrocatalyst nanoparticle size.
(iv) Reducing Pt dependence by developing metallic alloy (either as binary and ternary) and Pt-free electrocatalysts.
(v) Improving electrocatalyst dispersion by using novel fabrication methods.
(vi) Developing MEA (membrane electrode assembly) fabrication methods to enable better catalyst dispersion and utilisation.
(vii) Using new techniques to increase mass-transport at the fuel cell electrode surface.
(viii) Improving the performance of carbonaceous electrocatalyst support and exploring novel non-carbonaceous electrocatalyst support materials.

Among the wide variety of fuel cells, PEMFC and DMFC have been extensively studied over the last two decades or so [12–17]. These have emerged as one of the potential systems, which not only provide clean energy but also offer good commercial viability (e.g. Ballard and Smart Fuel Cells). A large number of successful applications of PEMFCs and DMFCs like passenger vehicles, generators (APU), chargers and other portable and hand held devices including mobile phones and laptops are currently commercially available [18–20]. However, despite the significant advances they still suffer from high-cost (mainly due to the catalyst) and durability issues.

Platinum (Pt) and Pt based alloys are the most commonly used catalysts for PEMFC and DMFC as Pt offers: (i) highest catalytic activity, (ii) chemical stability, (iii) high exchange current density (i_o), and (iv) superior work function [21–24]. However, the global scarcity of Pt and its high cost demand for an urgent need to reduce the use of Pt and to improve the efficiency in PEMFC and DMFC. Catalysts in PEMFC/DMFC are commonly supported on conductive and porous membranes. It is well known that supported metal catalysts show improved stability and higher activity compared to unsupported bulk metal catalysts. Surface area, porosity, electrical conductivity, electrochemical stability and surface functional groups characterise a support. An ideal support should offer the following: (i) good electrical conductivity, (ii) good catalyst–support interaction, (iii) large surface area, (iv) mesoporous structure enabling the ionomer and polymer electrolyte to bring the catalyst nanoparticles close to the reactants, i.e. to maximize the triple-phase boundary (TPB), (v) good water handling capability to avoid flooding, (vi) good corrosion resistance, and (vii) easy recovery of the catalyst [25]. A good interaction between the catalyst and the support not only improves catalyst efficiency and decreases catalyst loss but also governs charge transfer. The support can also assist in sufficiently enhancing the catalyst performance and durability by reducing catalyst poisoning (e.g. CO, S, etc.); and in some cases it affects the catalyst particle size. Hence, the choice of support material is vital and highly influential in determining the behaviour, performance, longevity and cost effectiveness of the catalyst and the overall fuel cell. In fact, it may be said that the approaches that have been adopted to achieve better catalyst efficiency can broadly be divided into the following categories: (i) employing Pt based bi-metallic and ternary catalyst systems and other non-precious metals to decrease Pt dependency and; (ii) improving the catalyst support. Furthermore, most of the feasible substitutes for Pt are other platinum group metals (PGM), including palladium, ruthenium, rhodium, iridium and osmium. These are no more abundant than Pt, making it all the more essential to reduce catalyst loading and improve efficiency [26]. Hence, an improved catalyst support capable of assisting and improving the catalyst performance in various ways as listed above is highly desirable.

Conventionally, highly conductive carbon blacks (CBs) of turbostratic structures with high surface areas, such as Vulcan XC-72R (Cabot Corp, 250 $m^2\,g^{-1}$), Shawinigan (Chevron, 80 $m^2\,g^{-1}$), Black Pearl 2000 (BP2000, Cabot Corp., 1500 $m^2\,g^{-1}$), Ketjen Black (KB EC600JD & KB EC600J, Ketjen International, 1270 $m^2\,g^{-1}$ and 800 $m^2\,g^{-1}$, respectively) and Denka Black (DB, Denka, 65 $m^2\,g^{-1}$) are currently used as fuel cell electrocatalyst supports to ensure large electrochemical reaction surfaces.

However, a multitude of materials other than CBs have been investigated as catalyst supports for PEMFCs and DMFCs. Over the last decade or so, the focus has shifted towards nanostructured supports as they enable faster electron transfer and high electrocatalytic activity. Broadly, these may be classified into two main categories: (i) carbon based/carbonaceous supports and (ii) non-carbonaceous supports. The first category consists of carbon nanostructures like mesoporous carbon, carbon nanotubes (CNTs), nanodiamonds, carbon nanofibers (CNF) and graphene [27–35c]. These nanostructured allotropes of carbon boast of essential fuel cell support properties like high specific surface area, high electrical conductivity and relatively good stability in acid and alkaline media. Catalyst supports that consist of carbon nanomaterials with higher graphitic nature (e.g. CNT and CNF) are reported to be more stable [36].

Among non-carbonaceous based materials, titania, indium oxide, alumina, silica, tungsten oxide nanostructures and conducting polymers have been widely investigated [37–50,206–210]. More recently materials like ceria and zirconia are also being explored [51–53]. The search for non-carbonaceous based supports is particularly essential to deal with the issue of carbon corrosion, which is suffered by all carbon supports (though in varying degrees). Corrosion of the support inherently leads to further issues like loss of catalyst, which drastically affects the overall performance of the fuel cell.

In this review, we discuss the performance, potential and issues associated with the use of various carbon and non-carbon based catalyst supports which are widely investigated for anode and cathode catalyst supports in PEMFC and DMFC.

2. Nanostructured carbon supports

Carbon blacks (especially Vulcan XC-72) are the most commonly used supports for Pt and Pt-alloy catalysts for fuel cells in many studies and commercial applications. These are usually prepared by pyrolysing hydrocarbons. CB consists of near-spherical particles of graphite, <50 nm in diameter. These coalesce into particle aggregates and agglomerates of around 250 nm in diameter. The particles have polycrystallite structures, which assemble to form non-discrete 3D groupings. Each crystallite consists of several 'turbostratic' layers with an interplanar spacing, of 0.35–0.38 nm. The source material and the process of its thermal decomposition largely determine the morphology and particle size distribution of CB [243]. The high surface area ($\sim$250 $m^2\ g^{-1}$ for Vulcan XC-72), low cost and easy availability of CBs help reduce the overall cost of the fuel cell. Although widely used as catalyst–support, CBs still suffer from problems such as (i) the presence of organo-sulphur impurities and (ii) deep micropores or recesses which trap the catalyst nanoparticles making them inaccessible to reactants thus leading to reduced catalytic activity. The pore size and pore distribution also affect the interaction between Nafion® ionomer and the catalyst nanoparticles. Since the size of Nafion® micelles (>40 nm) is larger than the recesses in the CB, any metal nanoparticles in pores with diameter lower than the micelle size are not accessible to Nafion® and provide no contribution to the electrochemical activity. Furthermore, CB is thermochemically unstable. Thermochemical stability is required under acidic conditions of a typical DMFC/PEMFC and the absence of this leads to corrosion of the carbon support resulting in disintegration of catalyst layer. Consequently, elaborate studies on CNTs, mesoporous carbon and CNFs have brought forth advantages like improved catalyst efficiency and higher ECSAs of the catalyst. These properties are highly desirable for reducing catalyst loadings thereby lowering the overall fuel cell cost.

2.1. Carbon nanotubes (CNT)

CNTs are 2-D nanostructures, typically tubes formed by rolled up single sheets of hexagonally arranged carbon atoms. They may be single walled (SWCNT) or multi-walled (MWCNT). Depending on the structure, SWCNTs can be conducting, i.e. metallic as well as semi-conducting in nature. SWCNT structure is characterized by a chiral vector (m, n) which defines its metallic or semi-conducting properties. All armchair SWCNTs ($n = m$) are known to be metallic. SWCNTs with $n - m = 3k$, where k is a nonzero integer, are semiconductors with a small band gap. All other SWNTs are semiconductors with a band gap inversely proportional to the nanotube diameter. MWCNTs can have diameters of a few tens of nanometers with a spacing of 0.34 nm between cylindrical walls. CNTs are the most well known and by far the most widely explored carbon nanostructures for application as catalyst support in fuel cells. Both SWCNTs and MWNTs have been extensively studied for PEMFC and DMFC catalyst support applications [54–57]. MWNTs have been found to be more conductive while SWCNTs provide larger surface areas.

Various methods (which were previously used with CB) like impregnation [58–60], ultrasound [61,62], polyol and microwave-assisted polyol [63–65], sputter deposition [66,67], precipitation [68], colloidal [69], ion-exchange [70,71] and electrochemical deposition (either pulsed or continuous) [72,73,57] have been widely explored for the deposition of the electrocatalyst nanoparticles on CNTs. Pristine CNTs are chemically inert making it difficult to attach metal nanoparticles. Thus, functionalisation to introduce surface oxygen groups (using strong acids like HNO_3, H_2SO_4, etc.) and others using ionic liquids have been performed commonly in order to make the surface more hydrophilic and improve the catalyst support interaction. First acid functionalised CNTs for deposition of the catalyst nanoparticles were reported in the late 1990s [74]. Since then the process has been continuously employed to obtain better dispersion of metal catalyst nanoparticles, better size control and distribution and also selective morphologies for application in DMFC and PEMFC. Surface modified CNTs have been used to support a wide variety of mono, binary (e.g. Pt–Ru, Pt–Co, Pt–Fe) as well as ternary catalyst (e.g. Pt–Ru–Pd, Pt–Ru–Ni, Pt–Ru–Os) systems using both noble and non-precious metals [27,29,57,60,75,77,77b]. For example, Tang et al. sputter deposited nanosized Pt nanodots (2–3 nm) as catalyst on CNT prepared *in-situ* on carbon paper. The system acting as a combined gas diffusion layer (GDL) and catalyst layer displayed a high maximum power density of 595 mW cm^{-2} using a catalyst loading of 0.04 mg cm^{-2} Pt on the cathode side. This was significantly higher than the Pt/Vulcan XC 72R-based electrode (435 mW cm^{-2}) with equal Pt loadings and that of the reference electrode with sputtered Pt on CNT/CB blend layer (530 mW cm^{-2}) [76]. Hsieh et al. studied the electrochemical activities of three types of Pt–Co/CNT catalysts, prepared from various Co depositions, in methanol oxidation reaction (MOR). These catalysts not only displayed different crystalline sizes but also different levels of atomic distribution. Two samples B1 and B2 were prepared using strong reducing agent ($NaBH_4$) which enabled the formation of a cobalt layer over the Pt surface, inducing bimetallic Pt–Co particles, whereas the third sample H1 was prepared using direct thermal reduction which enabled the formation of Pt–Co nano-alloy with a high degree of alloying (SEM shown in Fig. 1). Cyclic voltammetry (CV) studies revealed that sample with higher alloying degree (H1) exhibited a better electrochemical activity, high CO tolerance, and long-term durability (>100 cycles) [77].

Ahmadi et al. used sulphur modified CNT as Pt nanoparticle support for the MOR. In this study, no acid pre-treatment procedures were required to modify, i.e. functionalise CNT surface. Highly dispersed Pt nanoparticles were found to have narrow size distribution with an average size <3 nm. The elemental sulphur modified CNT was prepared using solvent impregnation method. Much higher current responses and long term stability was observed with respect to commercial Pt/C. The authors concluded that sulphur modification generated anchoring sites on the inert surface of the CNT without damaging the intrinsic conductivity of the CNTs that otherwise limits the overall electrocatalytic activity [78]. Park et al. performed accelerated stress tests on Pt supported on MWCNT to study their polarisation losses and electrochemical behaviour for PEM fuel cell cathodes. When compared to Pt supported on Vulcan XC-72, CNT based catalyst showed higher retention of electrochemical area, smaller increment in interfacial charge transfer resistance and a slower degradation of the fuel cell performance. This conclusively confirmed the higher corrosion resistance of MWCNT and also a stronger interaction with the Pt nanoparticles. It was also observed that highly corrosion-resistant MWCNT prevented the cathode catalyst layer from severe water flooding by maintaining the electrode structure and hydrophobicity for a long period under continuous anodic potential stress. Loss in catalytic sites available for oxygen reduction reaction (ORR) was found to be a major contributor to the overall overpotential [79].

Conjugated polymers such as polypyrrole (PPy) and polyaniline (PANI) form covalent bonds between Pt atoms and N atoms in PANI enabling strong adhesion of Pt nanoparticles onto PANI [80–83]. He et al. synthesised Pt nanoparticles on PANI functionalised MWCNTs where PANI acted as a bridge between Pt nanoparticles and CNTs (Fig. 2). PANI was found to wrap around the CNTs due to π–π bonding between CNT and PANI. Cyclic voltammetry studies and accelerated degradation tests revealed high electroactivity and excellent electrochemical stability displayed by Pt/MWCNT electrodes when compared to non-functionalised MWCNT and commercial CB supports [80].

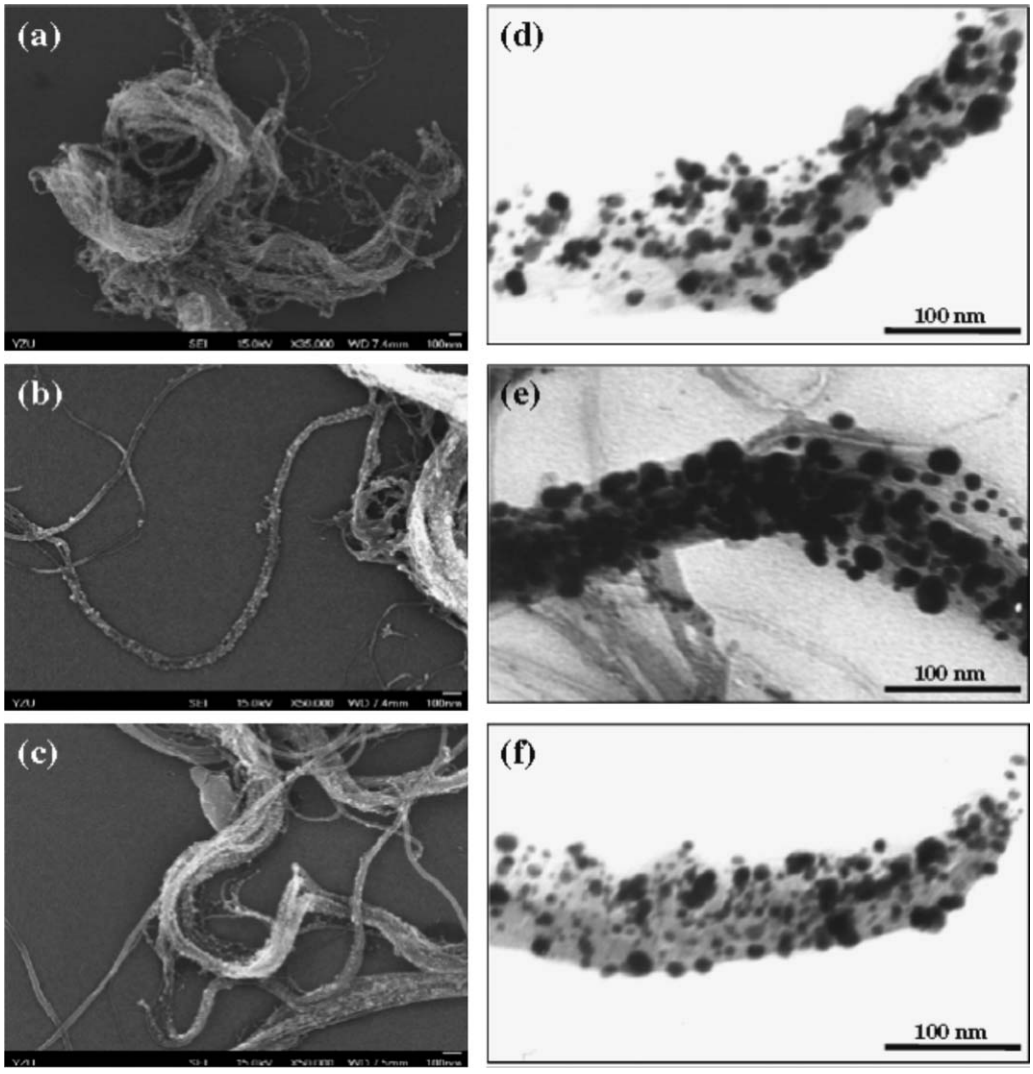

Fig. 1. SEM images of different Pt–Co/CNT samples: (a) B1, (b) B2, and (c) H1. TEM images of different Pt–Co/CNT samples: (d) B1, (e) B2, and (f) H1 [77].

Another technique to modify the surface of CNTs is to employ power ultrasound. It is well known that ultrasound enables formation of smaller and more uniform nanoparticles [62,84]. Yang et al. studied and compared the effect of using ultrasonic treatment and conventional reflux method on surface functionalisation of MWCNT. Pt–Ru nanoparticles were loaded onto two sets of MWCNTs using a colloidal method. Their studies revealed that the ultrasonically activated MWCNTs (25 kHz for 2 h) exhibited more

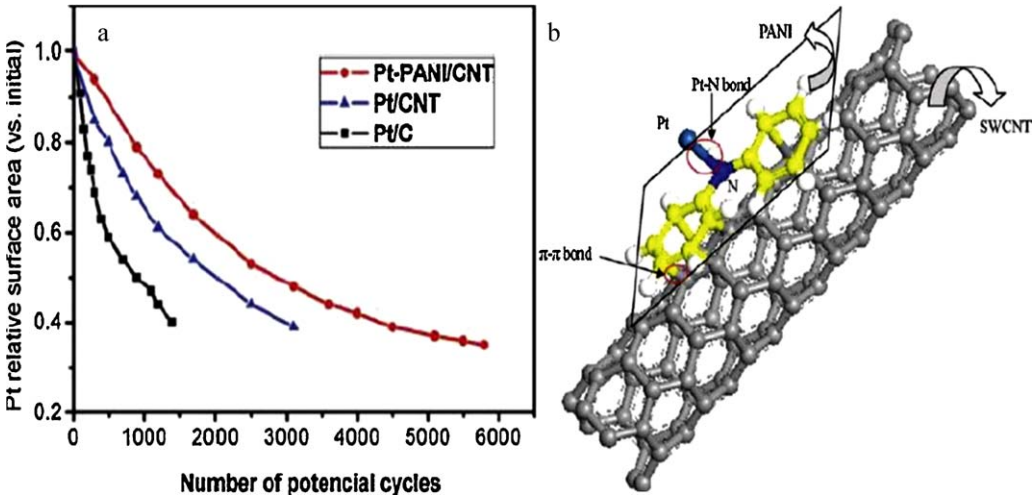

Fig. 2. (a) *ECSA* of the catalysts as a function of the number of potential cycles. (b) Schematic showing molecular interactions in the synthesized Pt–PANI/CNT catalyst [80].

uniform surface, shorter length, higher separation and openings and, modified surfaces with oxygen-functional groups, which favours Pt–Ru loading. Higher *ECSAs* and much improved CO-tolerance of electrocatalysts supported on ultrasonically treated MWCNTs were attributed to better dispersion and utilisation of Pt–Ru nanoparticles [62]. Xu et al. deposited Pt–Ru nanoparticles on ultrasonically treated MWCNT using an ultrasound (200 W, 40 kHz) induced HCHO reduction technique. The process enabled rapid and ambient temperature synthesis of highly dispersed Pt–Ru alloy nanoparticles. The observed high dispersion of electrocatalyst particles was mainly attributed to cavitation phenomena induced by ultrasonic irradiation; which not only prevented the further growth and aggregation of the Pt–Ru nanoparticles on the MWCNTs but also enabled isolation of MWCNT bundles [84].

The ability of nitrogen doped CNT (N-CNT) to facilitate the ORR was not reported until 2009 [85]. Since then the study of CNTs for use in PEM/DM fuel cell cathode has gained tremendous momentum [86–88]. Ghosh et al. prepared flower-like Pt nanostructures with an average size of 80 nm on MWCNTs. The system exhibited excellent ORR activity along with MOR activity [89].

One distinct advantage offered by MWCNTs is their significantly resistance towards corrosion compared to CB. The stability of the underlying carbon support affects the loss of platinum surface area following both platinum particle sintering and platinum release from the carbon support [244]. Voltammetric and XPS studies conducted by Shao et al. on MWCNTs synthesised using chemical vapour deposition provide a clear evidence of the resistance of CNTs towards electrochemical oxidation when these were exposed to conditions similar to those of a low temperature fuel cell. Since CNTs are rolled up co-axial sheets of graphene, oxygen atoms find it hard to attack this structure. On the other hand, carbon black contains mainly plane graphite carbon and amorphous carbon, which has an abundance of dangling bonds and defects [244]. The dangling bonds can easily form surface oxides, which results in a higher corrosion rate under electrochemical oxidation. Although CNTs also contain dangling bonds and defects, but these are much less than carbon black consequently CNTs are more stable in strongly oxidizing conditions [245].

Another study was conducted by Li et al., which focussed on the electrochemical stability of CNTs. their studies revealed that when attacked by the oxidative acids, only the outside graphene layers of MWCNTs were damaged, creating surface defects with edges on the CNT surface. The initial fast oxidation of CNTs was attributed to the defect carbons as it occurred both at the surface and at the ends. However, further oxidation must attack the intact basal planes beneath the defect carbons, which is difficult. In contrast, amorphous carbons and discontinuous graphite crystallites in CB provide ample sites for the electrochemical oxidation [246]. The architecture of the CNTs also gives rise to specific edge sites where the Pt crystallites can easily anchor. It has been shown in the literature that these sites are more active than the conventional sites obtained in CBs. The CBs possess sites which can be described as equi-potential sites and hence almost all the Pt sites are moderately active [247]. However, specific Pt crystallites sites anchored on CNTs provide active sites which are much more active.

It has been previously proposed that carbon supports with a higher graphitic component are much more thermally and electrochemically stable due to their higher corrosion resistance. Wang et al. [248] have compared the electrochemical activity and stability of as prepared (CVD-MWCNTs) and highly graphitized (HG-MWCNTs) Pt-modified CNTs. It is well known that the corrosion behavior of carbon support affects the stability of Pt/C catalyst. Coloma et al. [249] have reported that the formation of partial graphitization made the surface of carbon more resistant to air oxidation due to the π-complex structures (π-sites) in the carbon basal planes. These π-sites are formed when oxygen surface complexes are removed from the surface of activated carbon, e.g. by heat treatment in an inert atmosphere [249–251]. Electrochemical investigations have suggested that the HG-MWCNT have a lower corrosion rate than the original MWCNT, which can be attributed to the less surface defects on the HG-MWCNT with the increase of the graphitization degree. The high stability of HG-MWCNT results in the high stability of the Pt/HG-MWCNT catalyst. In addition, increasing the degree of graphitization leads to the increasing strength of π-sites (sp2-hybridized carbon) on the support, which act as anchoring centers for Pt, thus strengthening the metal–support interaction. The higher graphitic content has also been linked to a stronger interaction between metal and carbon support. Similar results were obtained by Kang et al. [252] in their study of high temperature heat treatment of activated carbon. Using Van-Dam's model for presence and interaction of ligand sites for Pt precursor on carbon support, they concluded that more π-sites were created when the heat treatment temperature was increased. This increase in the formation of π-sites was reflected in the increase of Pt^0 observed on the surface, leading to a higher oxidation resistance.

However, despite all the advantages offered by CNT, its application to fuel cells is still faced by many challenges. The current synthesis techniques for CNT are not suitable for large scale production and suffer from cost limitations. Although the costs of CNTs have reduced significantly over the last few years there is still a need to develop cost-effective methods for its large scale production.

2.2. Carbon nanofiber (CNF)

Carbon nanofibers (CNF) were first produced by the decomposition of hydrocarbons over metal particles. Rodriguez et al. reported the use of CNF as a catalyst support for Fe–Cu particles [90]. Since then these have been extensively researched as fuel cell supports [91]. The basic difference between CNTs and CNFs is that unlike CNT, CNFs either have a very thin or no hollow cavity. The diameters of CNFs are much larger than CNTs and may go up to 500 nm while the length can be up to a few millimetres. CNFs have been classified into three types: (i) ribbon-like CNF, (ii) platelet CNF and (iii) herringbone (or *stacked-cup*) depending upon the orientation of the nanofibers with respect to the growth axis. Herringbone CNFs are known to have intermediate characteristics between parallel and platelet types, thereby exhibiting higher catalytic activity than the parallel and better durability than the platelet forms [92].

Li et al. prepared Pt nanoparticles (5–30 wt.%) of 2–4 nm supported on *stacked-cup* CNFs (SC-CNFs) using the polyol process. MEAs based on Pt/SC-CNFs were prepared using a unique filtration process. The Pt/SC-CNFs-based MEA with 50 wt.% Nafion® displayed higher PEMFC performance than the commercial CB (E-TEK)-based MEA with 30 wt.% Nafion® content. The improved performance was attributed to high aspect ratio (length to diameter ratio) of CNFs which allows formation of continuously conducting networks in the Nafion® matrix [93]. Durability studies performed by Kang et al. on CNF supported Pt–Ru anode for DMFC revealed a constant current density of 150 mA cm^{-2} for approximately 2000 h [94].

Zheng et al. studied the effect of microstructure in CNFs on the ORR activity [92,95,96]. Sebastián et al. studied the influence of CNF support on ORR in DMFC. In this study, different temperatures were used to for the synthesis of herringbone CNFs with varying textural and crystalline properties. Microemulsion method was used to deposit Pt nanoparticles (2–3 nm) on the CNF support and performance was compared with that of commercial Pt/C (Vulcan XC-72R) with Pt nanoparticle size between 2 and 3.5 nm. Highly graphitic CNFs displayed better catalytic activity, despite its lower surface area and pore volume compared to CB [97]. Zhang et al. reported synthesis of submicrometer scale flat carbon fibres (SFCF)

using chemical vapour deposition (CVD) technique and studied the MOR activity of Pt/SFCF in comparison with Pt/C. Higher electrocatalytic activity was observed in both acidic and alkaline media which was attributed to the unique microstructure of the SFCF. In their studies, the fibres did not require any pre-treatment unlike other carbon supports [98].

Like CNTs, various functionalisations have also been attempted to improve the performance of CNF as support material [30,31]. Maiyalagan et al. used polyamidoamine (PAMAM) dendrimer functionalised CNF for MOR activity. Using the sodium borohydride ($NaBH_4$) method, Pt–Ru nanoparticles were deposited on the functionalised CNF and the performance of this conjugate was compared to commercial Pt–Ru/C (Cabot, Vulcan XC-72). Their studies revealed terminal enhanced activity and stability which was attributed to high dispersion of Pt–Ru nanoparticles (Fig. 3). The high dispersion was facilitated by terminal amine functional groups which provided uniform preparation of size monodisperse catalysts and assisted controlled dispersion [31].

One of the biggest differences between the CNTs and the CNFs is the exposure of the active edge planes. Unlike the CNTs where a predominant basal plane is exposed; only the edge planes which present potential anchoring sites (platelets and herringbone structure), are exposed in case of CNFs. Furthermore, various acid treatments also help to remove the residual metal impurities left behind during the synthesis of CNFs. Steigerwalt et al. [253] and Bessel et al. [254] demonstrated that CNF-supported catalysts showed improved methanol oxidation activity as compared to CB. Bessel et al. [254] found that catalysts consisting of 5 wt.% Pt supported on "platelet" and "ribbon" type graphite nanofibers exhibited activities comparable to that displayed by about 25 wt.% Pt on Vulcan carbon. Furthermore, they observed that the graphite nanofiber-supported metal particles were significantly less susceptible to CO poisoning than the traditional catalyst systems. This improvement in performance is believed to depend on the fact that the metal particles adopt specific crystallographic orientations when dispersed on the highly tailored graphitic nanofiber structures.

2.3. Mesoporous carbon

Mesoporous carbon materials belong to the class of porous carbon materials with pore sizes of 2–50 nm providing high surface area and conductivity. They can be classified into two categories on the basis of their final structure and method of preparation: (i) ordered mesoporous carbons (OMC) and (ii) disordered mesoporous carbon (DOMC). OMCs are prepared either by using ordered mesoporous silica templates or by templating triblock copolymer structures [99,100]. A wide range of applications have been explored for OMC including Li-ion batteries and fuel cells. They have also been widely studied as catalyst support materials for fuel cells [101–104]. It is commonly accepted that the structure of the carbon support is an important factor affecting the performance of the electrocatalyst. It determines the accessibility of the reactants to the catalytic site and also the removal of the products. The interesting morphological structure of MC, with large surface area and mono-dispersed mesospheres connected three-dimensionally facilitates diffusion of the reactants and by-products; thus making them very attractive materials as catalyst supports. The OMCs also enables efficient diffusion of hydrogen to the active catalyst sites. MC is also known to have some surface oxygen groups which are considered to improve the interaction between the metal catalyst and the carbon support allowing better dispersion.

Song et al. investigated the effect of pore morphology of OMC-CMK-3 as well as disordered worm-like mesoporous carbon (WMC) on the catalytic activity of Pt nanoparticles. The two structures were found to have similar pore size (~4 nm) and surface chemistry. In their work, 20 wt.% Pt was loaded on the two supports using pulse-microwave assisted polyol process to produce Pt/CMK-3 and Pt/WMC. XRD studies and TEM images revealed that Pt nanoparticles of size ~3.1 nm (CMK-3) and 3.2 nm (WMC) were uniformly dispersed on the pore surface of both samples. However, Pt nanoparticles on CMK-3 appeared to possess more electrochemically active sites and also higher electrochemical active surface area. Pt/CMK-3 exhibited superior ORR activity which was attributed to its highly ordered structure and good 3-D interconnection of the nano-spacings of their hexagonally arranged carbon nanorods enabling catalysts to possess higher catalyst utilization efficiency compared to WMC. The authors concluded that pore morphology along with pore structural parameters and surface chemistry played in important role in porous materials. They also concluded that desired pore morphology can enable easier mass transportation which is much more prominent in case of liquid reaction [32]. The choice of template (hard or soft) used to synthesis OMC also appears to make a difference to its electrochemical performance [105]. Calvillo et al. studied the effect of surface chemistry of the OMC-CMK-3 support on the synthesis and performance of Pt electrocatalysts. OMC prepared using the nanocast method was functionalised using HNO_3 to modify its surface chemistry. The oxidation treatment was carried out in concentrated as well as dilute (2 M) HNO_3. Pt nanoparticles were deposited on it using an incipient wetness impregnation method in order to decrease the hydrophobicity of the support and improve catalyst–support interaction. The nitric acid treatment affected the morphological and textural properties of the support due to the introduction of various surface oxygen groups. Interestingly, it was found that the highly ordered structure of the support was not affected which was confirmed by XRD and TEM studies. The average size of the Pt nanoparticles on the CMK-3 supports, treated with dilute HNO_3, was found to be in the range of 7.0–8.0 nm. However, much larger particle sizes (22.3–23.3 nm) were observed for CMK-3 supports treated with concentrated HNO_3 demonstrating the effect of surface chemistry on the support. The decrease in surface specific areas and pore volumes along with significant increase in surface oxygen groups led to sharp increase in metal nanoparticle size. TEM images also revealed more agglomeration of metal nanoparticles on highly functionalised CMK-3. N_2 adsorption–desorption isotherms revealed lower specific surface area and total pore volume for CMK-3 support compared to 'conventional' carbon support. Polarisation and power density curves (Fig. 4) exhibited better electrocatalytic behaviour for CMK-3 based electrodes (13–27 mW cm^{-2}) compared to commercial *E-TEK* electrodes (9.5 mW cm^{-2}), despite lower electrical conductivity of CMK-3 and larger Pt nanoparticle sizes. It was also observed that ohmic and mass transfer polarisation losses were more significant for highly functionalised support samples. This was attributed to decreased electrical conductivity, higher agglomeration and lower specific surface area [106–108]. Liu et al. explored the effect of large pore size and a broad pore size distribution (10–100 nm) in DOMC used as PEMFC catalyst support. In their investigation, 18 wt.% Pt/MC was used to prepare MEAs and their performance were compared to that of commercial 20 wt.% Pt/C. Here, Pt nanoparticles on MC supports were larger and more agglomerated. The authors addressed the issue of pore volume in catalyst ink formulations, and the importance of ionomer inside mesopores. It was also observed that MEA with Pt/MC and Nafion® ionomer/binder could not be prepared using conventional catalyst ink formulations by the decal transfer method, due to Nafion® being taken up inside MC pores. The lower performance of the Pt/MC compared to Pt/C was attributed to larger particle size and lack of good contact between Pt nanoparticles and Nafion® buried inside the large pores of MC [107].

Bi-metallic catalyst systems have also been investigated with OMC [106,109,110]. Salgado et al. synthesised Pt–Ru electrocatalyst

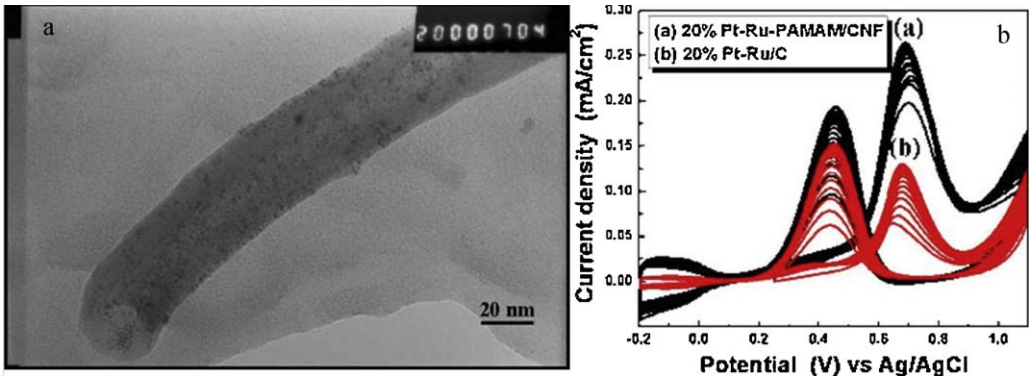

Fig. 3. TEM image of 20% Pt–Ru–PAMAM/CNF catalyst. Cyclic voltammogram of (a) Pt–Ru–PAMAM/CNF and (b) Pt–Ru/C in electrolyte solution of 0.5 M H_2SO_4 with 1 M CH_3OH at a sweep rate of 50 mV s^{-1} at room temperature [31].

supported on CMK-3 to study the performance in DMFC. Pt–Ru nanoparticles were deposited on CMK-3 using the formic acid reduction method. The performance of as-prepared electrocatalyst was compared with Pt electrocatalyst supported on Vulcan XC-72 and commercial Pt–Ru/C from *E-TEK*. EDX was used to determine the atomic composition of Pt:Ru as 85:15 in CMK-3 supported samples and 50:50 in commercial samples. The Pt–Ru/CMK-3 was found to demonstrate higher MOR activity compared to Vulcan carbon support. It also showed a shift (~0.15 V), in the CO-stripping potential towards more negative values indicating faster electron transfer kinetics [106]. Alloys of Pt with other non-precious metals have also been studied on OMC support [111].

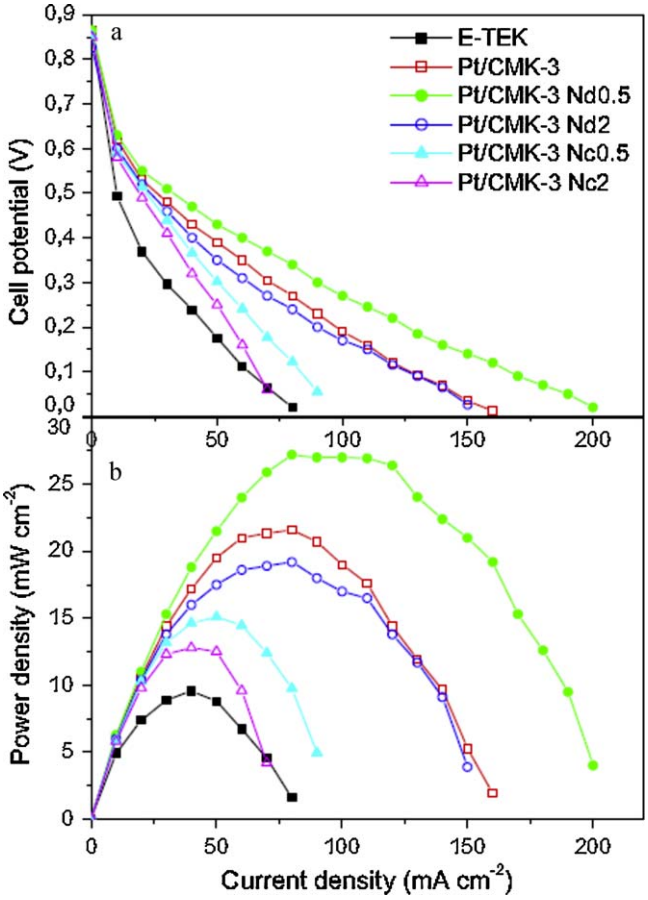

Fig. 4. Polarisation (a) and power density (b) curves of Pt electrocatalysts supported on CMK-3 carbons with different surface chemistry at the anode side in a PEM fuel cell working at room temperature and atmospheric pressure [108].

Similar to other carbon nanomaterials, OMC have also been doped with nitrogen and investigated for the ORR [112,113]. Liu et al. fabricated N-doped ordered mesoporous graphitic arrays (NOMGAs) using a metal-free nanocasting method. A very narrow pore-size distribution of ca. 3.8 nm was observed. NOMGAs with moderate nitrogen content provided a high surface area and a graphitic framework, leading to high electrocatalytic activity, excellent long term stability, and resistance to methanol crossover effects for the ORR compared to commercial Pt/C [114].

2.4. Nanodiamonds and doped diamonds

Undoped diamond is an electrical insulator with a band gap >5 eV. Boron (for p-type), phosphorous or nitrogen (for n-type) are common dopants. Boron has a low charge activation energy (0.37 eV) which makes it the most popular dopant. Boron doped diamond (BDD) films have been extensively investigated for applications as support for fuel cell catalyst [33–35]. BDD is highly desirable as a support material due to its wide electrochemical potential window in aqueous as well as non-aqueous media, and high electrochemical stability and corrosion resistance under both acidic and alkaline conditions [115–117].

Various different routes such as co-deposition of Pt with BDD during CVD growth [118], implantation into BDD [119], thermal decomposition on BDD [34] and electrochemical deposition on BDD [120,121] have been explored to optimise the process of Pt deposition on BDD. Salazar-Banda et al. studied the performance of Pt and other bi-metallic catalyst (Pt, Pt–RuO_2, Pt–RuO_2–RhO_2, Pt–SnO_2 and Pt–Ta_2O_5) deposited on BDD support using sol–gel synthesis. It was found that these electrodes offer long term stability and high corrosion resistance [122–124]. Lu et al. recently studied the performance of Pt–Ru alloy nanoparticles electrodeposited on BDD. Potentiostatic method was used to simultaneously deposit Pt–Ru at various working potentials, and the deposits were compared with those from sequential deposition. The electrocatalytic performance of the electrodes obtained from the two deposition methods were compared to the findings on the highly ordered pyrolytic graphite (HOPG) electrode. Pt–Ru electrodeposits from simultaneous deposition showed more stable CVs in sulphuric acid. The method also resulted in higher Ru content, and could also be controlled by a choice of the electrodeposition potentials such that more negative the deposition potential the lower the Ru content. These electrodes also exhibited higher activity and CO tolerance for MOR. It was also observed that while methanol dehydrogenation dominated at lower overpotentials, CO_{ads} oxidisation dominated at higher overpotentials [125].

La-Torre-Riveros et al. fabricated dimensionally stable, high surface area support from commercial diamond nanoparticles through

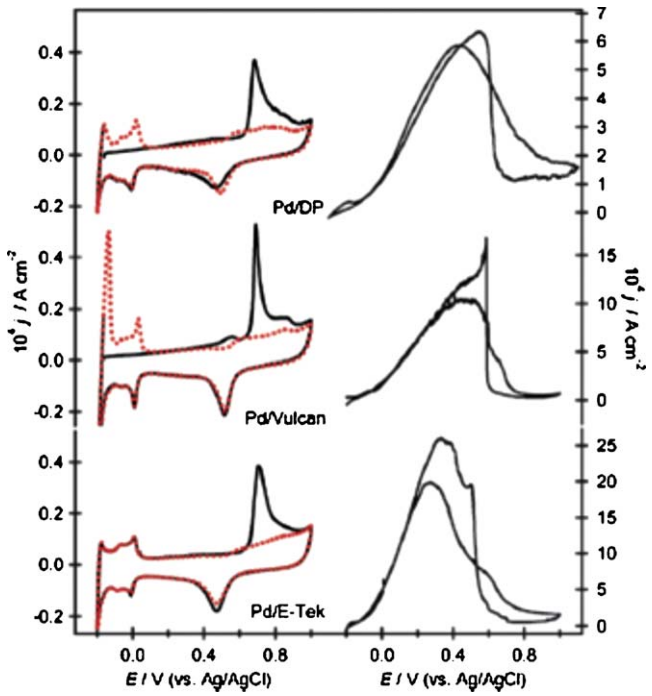

Fig. 5. CO stripping voltammograms (left) obtained for the Pd/DP, Pd/Vulcan and *E-Tek* electrocatalysts, at 0.02 V s^{-1}, in 0.5 M H_2SO_4. Formic acid (2 M) oxidation (right) was studied, under similar conditions, on the three electrocatalysts [127].

electrophoretic deposition onto silicon wafer substrates, and examined their electrochemical characteristics by employing inorganic redox probes such as the *quasi*-reversible systems $[Fe(CN)_6]^{3-/4-}$ and $[Ru(NH_3)_6]^{3+/2+}$. Layers of variable thicknesses were synthesised by altering applied voltage, deposition time and the diamond nanoparticle concentration in the solution. The authors found that the as fabricated layers were of homogeneous thickness and without macroscopic cracks or holes. Pt clusters were successfully deposited from the aqueous precursor complex solution using step and sweep potential method. MOR studies revealed that higher current was achieved for electrodes produced with lesser number of electrodeposition cycles which was attributed to the agglomeration of Pt nanoparticles on the nanodiamond support. However, the authors suggested that this methodology could be applied for future boron-doped nanodiamond catalyst support materials for fuel cell applications [126].

Although doping improves the conductivity of the diamonds, it can inversely affect its stability. Keeping this in mind, an interesting study was recently conducted [115] by Moore et al. which revealed that Pd nanostructures supported on highly crystalline, insulating diamonds (Fig. 5) can be potential electrocatalysts for fuel cells. The authors observed that Pd centres appeared interconnected to the electrode surface despite the inherent bulk resistivity of diamond nanoparticles. This was attributed to the possible hole mediated surface transport characteristic of hydrogenated diamond surfaces. Their study further demonstrated the possibility of using material such as high pressure, high temperature diamond powders as electrocatalyst support [127].

2.5. Graphene

Graphene is an atomically thin sheet of hexagonally arranged carbon atoms which has attracted a lot of interest since its discovery by Geim et al. in 2004 [128]. It offers high conductivity and one of the fastest available electron transfer capabilities. As such, it is widely studied for various applications including, fuel cell catalyst support. The use of graphene and its oxide (graphene oxide – GO) in fuel cell is not only limited to that of catalyst support but it is also being explored as material for (i) conducting membranes as a composite with polymers and also as (ii) bipolar plate material [129]. However, this discussion is beyond the scope of this review.

Graphene has aroused interest as potential support owing its high electron transfer rate, large surface area and high conductivity [130–133]. The 2-D planar structure of the carbon sheet allows both the edge planes and basal planes to interact with the catalyst nanoparticles. The rippled but planar sheet structure also provides a very high surface area for the attaching catalyst nanoparticles.

Soin et al. explored the use of vertically aligned graphene nanoflakes (FLGs) for the MOR. The FLGs were grown using microwave plasma assisted chemical vapour deposition on a silicon substrate. The structures were found to have highly graphitized terminal planes of 1–3 layers of graphene. Raman spectroscopy revealed very narrow full width half maxima (FWHM) for *G* and 2-D bands and an $I_G/I_{G'}$ ratio of 1, which confirmed the characteristics of highly crystallized few layered graphene. Pt nanoparticles were deposited on the FLGs using sputtering technique. CV curves demonstrated fast electron transfer (*ET*) kinetics for the Pt/FLG electrodes (SEM and CV curves in Fig. 6). This was ascribed to the highly graphitised edge structure of FLG nanoflakes. MOR studies also showed that Pt/FLG exhibited high resistance to CO poisoning compared to Pt/C [132]. In another study, Liu et al. reported synthesis of Pt nanoparticle-deposited expandable graphene sheet (Pt/EGS). The graphene sheets were fabricated on conductive ITO (indium tin oxide) glass electrodes electrochemical synthetic route [130].

The fast electron transport mechanism offered by graphene can particularly facilitate the ORR much more quickly and effectively in fuel cells. Nitrogen doped graphene has been shown to yield promising results especially for the sluggish cathodic ORR [131,134]. The disorders and defects introduced in the graphene stack due to the incorporation of nitrogen are known to act as anchoring sites for the catalyst nanoparticles [135,136]. Jafri et al. used nitrogen doped graphene nanoplateletes as Pt nanoparticle support for electrocatalytic studies. Graphene nanoplatelets were synthesised by thermal exfoliation of graphitic oxide and further treated in nitrogen plasma to produced nitrogen doped (3 at.%) graphene nanoplatelets. Pt nanoparticles were dispersed on the support using the sodium borohydride reduction process. MEAs fabricated using Pt/N-G and Pt/G as the ORR catalyst showed a maximum power density of 440 mW cm^{-2} and 390 mW cm^{-2}, respectively. The improved performance of Pt/N-G was attributed to the formation of pentagons and heptagons due to the incorporation of N in the C-backbone leading to increase in the conductivity of neighbouring C atoms [136].

Graphene's oxidised counterpart, i.e. GO, has also drawn a lot of interest and attention. Although GO has lower conductivity (a difference of two to three orders of magnitude compared to graphene), it offers a different set of properties (hydrophilicity, high mechanical strength, chemical 'tunability') compared to graphene, which makes it suitable for a wide range of applications. Moreover, variable oxygen content enables tunable electronic conductivity for various applications [137–140]. The use of GO as catalyst support material in PEMFC and DMFC is one of the latest applications of GO which have shown promising results [141–144]. Oxygen groups introduced into the graphene structure during the preparation of GO create defect sites on surface as well as edge planes. These defect sites act as nucleation centres and anchoring sites for growth of metal nanoparticles. Sharma et al. recently reported the synthesis of Pt nanoparticle on GO using the microwave assisted polyol method. The process allowed simultaneous partial reduction of GO and growth of Pt nanoparticles on reduced GO (RGO) support. The TEM studies of Pt/RGO revealed Pt nanoparticles of good control over particle size and distribution. Apart from high catalytic mass

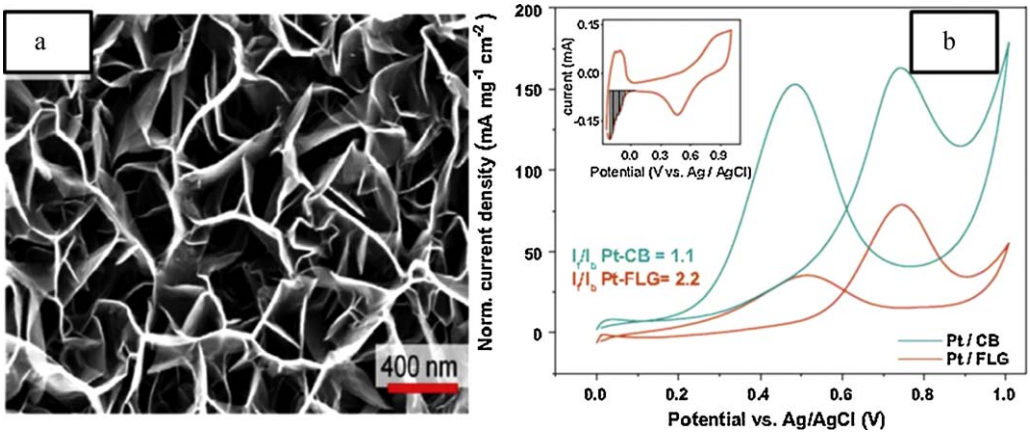

Fig. 6. (a) High magnification SEM image showing large density of nanoflakes. (b) Cyclic voltammograms in Ar saturated 1 M H_2SO_4 + 2 M CH_3OH performed at a scan rate of 50 mV s^{-1} for Pt–FLGs and Pt–CB. Inset: CV at a scan rate of 50 mV s^{-1} in 1 M H_2SO_4 for Pt–FLGs. The shaded portion represents hydrogen-desorption area used to calculate *ECSA* [132].

activity, higher electrochemically active surface area, MOR studies revealed I_f/I_b ratios as high as 2.7 compared to 1.3 for Pt/C. The strong 'anti-poisoning' behaviour was attributed to the presence of covalently bonded residual oxygen function groups on the RGO support. The authors clearly observed in linear dependence of I_f/I_b ratio on the concentration of residual oxygen species present in the RGO support (Fig. 7). The authors suggested the possibility of a bi-functional mechanism between Pt and the RGO support, and/or a possible hydrogen spillover effect which is commonly observed in Pt/WO_3 systems [142]. Ha et al. recently reported the use of Pt nanoparticles embedded on reduced GO for ORR in DMFCs. The authors used a modified polyol process to deposit ~2.9 nm Pt nanoparticles on reduced GO to produce 70 wt.% Pt/RGO. ORR studies and single cell polarisation studies were performed which demonstrated an 11% higher maximum power density for Pt/RGO compared to commercial (75 wt.%) Pt/C. After long-term stability the average particle sizes of Pt/C and Pt/RGO increased from 4.1 to 5.4 nm and 2.9–3.7 nm, respectively suggesting lower Pt agglomeration which would encourage mass transport by facilitating reactants to the catalytically active sites [145]. Other precious metal nanoparticles and bimetallic systems have also been grown on GO support and have exhibited superior catalytic activity [146].

2.6. Interaction between carbon support and catalyst

The carbon support plays a vital role in the preparation and performance of the catalysts as it enhances the catalyst dispersion and provides an underlying framework for electron conduction and gas diffusion. The underlying support affects the catalytic properties due to a variety of reasons including: (i) influencing the shape, size and dispersion of the catalyst nanoparticles, (ii) electronic interactions between support and catalyst [255,256]. The carbon support is characterized by fragments of basal and edge planes which are exposed to the surface. A surface that is built up solely of basal planes is uniform energetically and is considered as a homogeneous surface whereas a mixture of the edge and basal planes is considered as a heterogeneous surface [257,247]. Both theoretical and experimental observations indicate that the heterogeneous surface can better stabilize the metal in a highly dispersed state. In this condition, the metal particles are arranged on the carbon surface along the edges of graphene network at inter-crystalline boundaries or at edge steps. Previous results using Pd/C catalysts have shown that with an increase in the heterogeneity of the carbon support the dispersion of the catalyst particles increases [258]. The stabilization of the catalyst nanoparticles on the carbon surface involves the equalization of their respective Fermi levels and giving rise to a contact potential. The charge on the metal particle is strongly dependent on the nature of the carbon support, presence of adsorbates and crystallite size as well. There is a wide variety of literature showing that the Pt particles may acquire a negative or a positive charge [259–261]. A phenomenological description of this kind of metal–active carbon interaction was given by Hegenberger et al. [262]. According to this model, the charge transfer (from metal to carbon support) will be roughly equal in value to the number of surface state in the energy gap of the surface of the carbon support. It can be further deduced that the charge transfer from a metal particle to the support and consequently the stability of metal particles to sintering will increase with the number of

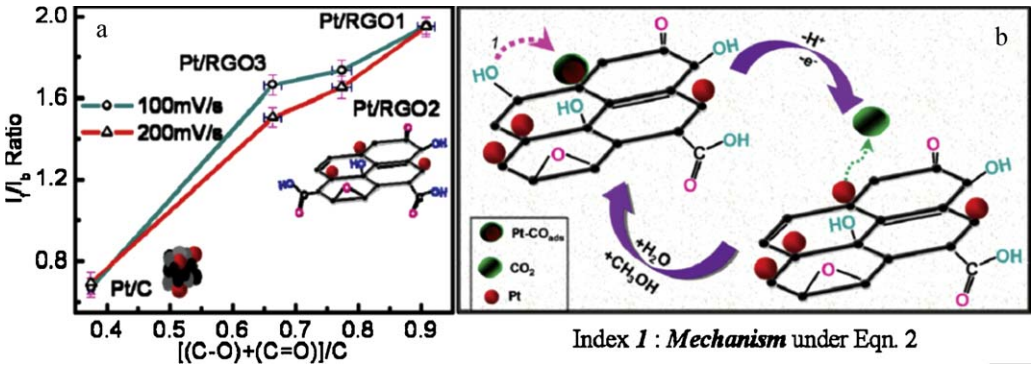

Fig. 7. (a) Dependence of I_f/I_b ratio on contribution of residual oxygen species. (b) Schematic diagram explaining the conversion of adsorbed CO_{ads} species to CO_2 on Pt/RGO hybrids representing suggested mechanism facilitated by residual oxygen groups [142].

surface carbon atoms with uncompensated bonds. It has been previously reported that at graphitic surfaces, transition metal atoms are mobile in nature and form clusters as the cohesive energy of these metals is much higher than the adsorption enthalpy. This formation of nanoparticles on graphitic surfaces such as CNTs, CNFs and Vulcan carbon is characterized as diffusion limited aggregation where the nucleation sites are comprised of defects, which can be either chemical or structural in nature [263]. In their study of deposition of Pt nanoparticles on Carbon Nanofibres (CNFs) and Ordered Mesoporous carbon (CMK-3), Calvillo et al. [264] reported that the size of Pt crystallites supported on CNFs was around 3 nm, whereas those supported on CMK-3 were approximately 7.6 nm. Since the catalysts were prepared by the same reduction method and with the same metal loading, the difference in the crystallite size can be attributed to the effect of support. It was observed that the higher crystalline grade support, provided a smaller Pt crystallite size. This effect has been attributed to the metal–support interaction [254,265], which is related to the nature of the support and has been considered to affect the growth, the structure and the dispersion of metal particles [255,260] The electronic interactions at the Pt–C interface modify the electronic structure of the metal and also affect the crystalline structure of the metal. The metal particles supported on CNFs showed a highly crystalline structure, associated with a strong metal–support interaction [255] whereas, Pt particles supported on Vulcan and CMK-3 adopted a more dense globular morphology associated with a weak metal–support interaction [264]. Similar results were obtained by Salgado et al. in their study of Pt and Pt–Ru electrocatalysts on CMK-3 and Vulcan carbon [266]. Thus, it can be clearly said that there is a reduction of the clusters size a better dispersion observed on highly crystalline surfaces can be attributed to a higher density of well-dispersed nucleation centers created.

The electronic interactions occurring between the catalyst nanoparticles and support have been investigated using a variety of spectroscopic techniques such as X-ray photoelectron spectroscopy (XPS) and extended x-ray absorption fine spectroscopy (EXAFS). It is well accepted that during a transition from bulk to nanoparticle domain, the electronic structure of the metal atom changes due to the de-hybridization of the spd metallic orbitals. This in turn results in an increased electronic density between the atoms thereby contracting the interatomic distance which can be probed using EXAFS. Also, depending upon the acidity/basicity of the underlying support, the electronic properties of catalysts can be tuned via electron transfer to/from the support and can be seen as pronounced shifts in the XPS spectra [267–269]. The effect of small metal nanoparticles also produces a line broadening and a shift to higher binding energy (*vs.* bulk) in the XPS spectra and has been associated with a stronger Pt–support interaction [270]. The metal particle size and nature of metal–support interaction of homogeneous deposition precipitation prepared Pt-oxygenated CNF and Pt-Vulcan XC-72 have been studied by Zhang et al. using EXAFS [271]. The structure of layered graphite provides two different surfaces, namely, prismatic (edge) surfaces and basal plane surfaces. The structure of metal–support interface on carbon-supported metal particles depends on the morphology of the surface on which the metal atoms are anchored. The physicochemical properties of CNFs and Vulcan-XC 72 are quite different to each other (i.e. a fishbone structure, higher surface area, and higher purity for CNFs). The oxygen-containing groups have a strong influence on the hydrogenation properties of Pt/CNF catalyst and remain stable even under a reducing atmosphere at 200 °C [272]. For Pt–CNFs, a EXAFS first Pt–Pt shell coordination number of 5.5 was measured whereas for Pt–Vulcan, the Pt–Pt shell coordination number is 8.2. This has been attributed to the nature of the metal–support interaction which involves a charge rearrangement from the Pt atoms in the metal–support interface to the center of the Pt cluster when the support oxygen atoms have higher electron richness (increase in basicity). Using a structural model, the authors have argued that the modification of the carbon surface with oxygen groups is crucial for the deposition of small metal particles. In a similar study, Bittencourt et al. have employed XPS and valence band XPS to study the evolution of Pt nanoclusters on pristine and oxygen plasma treated CNTs. With the increase in the Pt cluster size, the XPS spectra showed a shift in the 4f core level with an increase in the asymmetry. This was accompanied by the movement of the 5d states moved towards the Fermi level.

Traditionally, materials such as carbon black have been used extensively due to their high availability and low cost. In order to increase the anchoring sites for promoting metal loading and dispersion, chemical activation of CB is carried out. However, the inherent problems associated with them include high micro and nanoporosity leading to a reduction of catalyst utilization and low thermal and electrochemical stability. The high surface area and tailored meso-porosity of OMCs allows high metal dispersion and good reactant flux for PEMFCs. When compared to conventional CBs, the OMCs provided higher catalytic activity and higher thermal and electrocatalytic stability. Other supports such as CNFs do not require any chemical pretreatment due to the presence of highly active edge planes on which the catalyst nanoparticles can be attached. The advantage of high thermal and electrochemical stability of BDDs can be best exploited if new anchoring strategies using Nafion for attachment of catalysts can be developed. With the advent of advanced one and two-dimensional carbon supports such as CNTs and graphene, the problems associated with the nanoporosity and low utilization of catalyst have been overcome to a certain extent. The high crystallinity and surface area of CNTs and graphene provide a suitable support for the dispersion of catalyst nanoparticles. Under long-term durability tests, while the CBs underwent a morphological transition to induce catalyst aggregation, no such effects were observed for CNTs. The use of graphene supports provides high electron transfer rate along with high conductivity and the two-dimensional nature allows both the edge and basal planes to interact with the catalysts. Graphene and CNT based supports provide substantial advantages concerning mass and charge transport by providing shorter effective lengths for electronic and ionic transport. This in conjunction with a higher electrode/electrolyte interfacial area can enhance the efficiency and capacity of fuel cells. For the advanced nanostructured carbons such as CNTs, graphene or mesoporous carbon to completely replace the CB as catalyst supports, further and extensive testing of fuel cells especially with respect to electrochemical activity and long-term stability need to be carried out.

3. Non-carbonaceous and inorganic oxide/carbide supports

The use of nanostructured carbon materials have definitely improved the performance of the catalyst supports used in PEMFC as they exhibit strong influence on the catalyst durability and behaviour. Unfortunately carbon corrosion still exists for these systems. Although the undesirable reaction has no doubt been significantly reduced but the complete elimination of carbon corrosion is not yet achievable. Furthermore, functionalisation of the carbon support is used to improve the anchorage of the catalyst nanoparticles on the support and reduce agglomeration. However, functionalisation of the carbon support can make it more susceptible to electrochemical oxidation leading to loss of active surface area. It can also affect the ionomer distribution thereby affecting proton conductivity of the fuel cell electrodes [147]. Consequently, there is an urgent requirement to explore other non-carbonaceous supports to address these issues. The inertness of non-carbonaceous oxide supports such as TiO_2 or WO_3, makes

them materials very attractive for applications in relatively strong oxidative conditions, for example at the cathode of a working fuel cell [181]. Recently, Lewera et al. performed detailed X-ray photoemission spectroscopy studies on TiO_2 and WO_3 supported Pt to study the strong metal support interactions (SMSI) offered by these non-carbonaceous supports. They selectively photodeposited Pt on the TiO_2–C and WO_3–C composites. This enabled the investigation of the changes in the electronic properties of Pt and the support. They identified that the binding energy of the Pt 4f signal for platinum deposited on an oxide support was significantly lower when compared to that of Pt supported onto carbon. The increase in Pt 4f XPS signal asymmetry was observed which suggests an increased electron density on Pt. No electron donor was identified from the analysis of the oxide supports. In order to explain this observation, the authors suggested the possibility of two effects: (i) change in lattice energy due to alloy formation between Pt and the oxide support and (ii) partial charge transfer from substrate/oxide to Pt, which can be correlated to previously observed increased activity toward oxygen reduction reaction. The increased electron density on Pt also enhances the electrocatalytic activity of the Pt–support system towards ORR [273]. This section deliberates on the various non-carbonaceous: metal oxides/carbides and conducting polymers which have gained a lot of interest over the last few years [36–47,49,50,206–210].

3.1. Ti-based compounds

3.1.1. Titanium oxides (TiO_{2-x} or Ti_nO_{2n-1})

Titanium oxide or titania materials have been widely used as conductive metal oxides due to their excellent corrosion resistance in various electrolyte media. They exhibit very good photoelectrochemical (PEC) as well as electrocatalytic properties. The high corrosion resistance and electrochemical stability demonstrated by these oxides even in acids have encouraged studies of these as catalyst supports in fuel cells [148,36]. Additionally, they are cost-effective, non-toxic and easily available [149]. Titania can exist in three main crystallographic forms: rutile, anatase and brookite. Anatase titania is known to be more efficient as a photocatalyst than rutile. Stoichiometric titania (band gap 4.85 eV) is resistive and the presence of Ti^{3+} ions is essential for electronic conductivity. Ti^{3+} ions can either be generated by (i) creating oxygen deficiency by heating TiO_2 in reducing atmosphere (to obtain TiO_{2-x} or Ti_nO_{2n-1}) or (ii) introducing dopants. However, sub-stoichoimetric titania when exposed to fuel cell conditions becomes stoichiometic and forms a resistive TiO_2 layer at the three phase reaction interface [150,151].

Kim et al. studied the additive affect of TiO_2 based support for Pt electrocatalyst on the ORR activity. The authors described a unique way to modify the electronic characteristics of TiO_2 supports. Various additives, such as urea, thiourea, and hydrofluoric acid were used to modify the shape of TiO_2 particles using hydrothermal treatment. Pt nanoparticles were supported on TiO_2 support using the borohydride reduction process. Detailed TEM studies were performed on the samples and it was found that the hydrothermal treatment with different additives not only affected the shape of TiO_2 particles but also the dispersion of the Pt nanoparticles on the support. HF was found to be most effective additive in modifying the shape of TiO_2. HF treated TiO_2 support samples were found to have more round shapes and the supported Pt nanoparticles were more uniformly dispersed with a smaller particle size compared to other samples. The electronic states of different TiO_2 supports were also investigated using XPS and it was observed that HF treated Pt/TiO_2 had the highest relative intensity of Ti^{2+} or Ti^{3+}state. These acted as an electron donor and thereby improved the electronic characteristics on the surface of TiO_2 supports. XRD studies revealed that additive treated TiO_2 supports had smaller

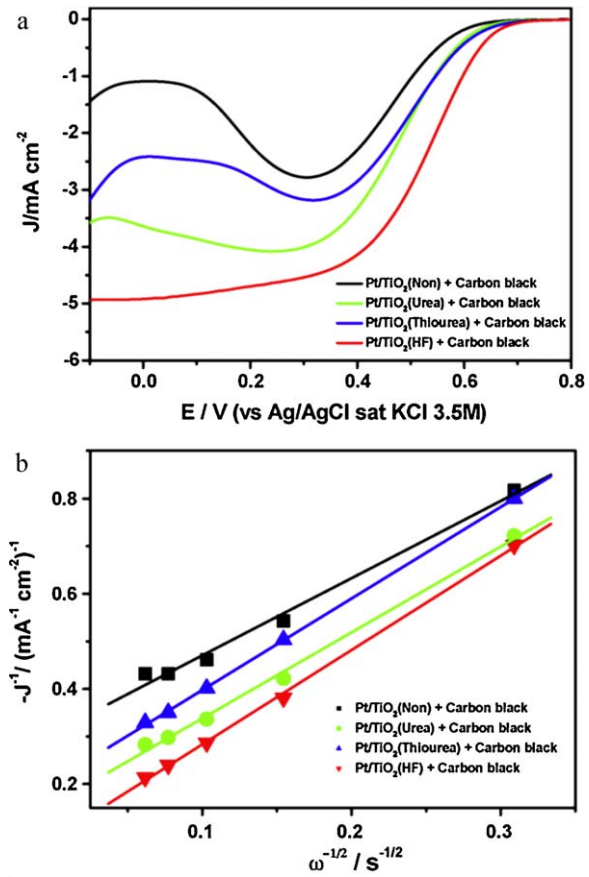

Fig. 8. ORR (a) of the various Pt/TiO_2 + carbon black electrocatalysts in oxygen saturated 0.1 M $HClO_4$ solution at a rotating speed of 1600 rpm and scan rate of 5 mV s^{-1}. Koutecky–Levich (K–L) plots (b) for ORR on the various Pt/TiO_2 + carbon black electrocatalysts at +0.4 V [152].

Pt nanoparticle and larger surface area compared to non-additive treated TiO_2 supports. Electrochemical studies showed that the order of ORR activity in various samples was in accordance with the band gap narrowing, in the following sequence: Pt/TiO_2 (no additives) + carbon black < Pt/TiO_2 (urea) + carbon black < Pt/TiO_2 (thiourea) + carbon black < Pt/TiO_2 (HF) + carbon black (Fig. 8) [152]. Huang et al. also prepared titania supported Pt electrocatalyst for PEMFC cathode. High surface area (266 m^2 g^{-1}) mesoporus TiO_2 were synthesised using a template assisted method. Uniformly distributed Pt nanoparticles with a size distribution of 3–5 nm were observed on TiO_2 nanoparticle (7–15 nm) support by TEM studies. 40 and 60 wt.% Pt/TiO_2 electrocatalyst were prepared. Accelerated degradation test (ADT) studies revealed 10-fold higher ORR for Pt/TiO_2 compared to commercial Pt/C (45.9 wt.% TKK). Pt/TiO_2 also showed high durability with only a small voltage loss after 4000 potential cycles (in the potential range of +0.0 to +1.2 V *vs.* RHE) while Pt/C suffered severe corrosion loss and showed no activity after 2000 potential cycles. No noticeable change in Pt particle size was observed for Pt/TiO_2 as opposed to a 3-fold increase in size (from 2.5 to 8 nm) due to agglomeration in the case of Pt/C. The authors concluded that Pt/TiO_2 was found to be highly durable and stable as cathode catalyst for PEMFC [153].

Wang et al. studied the performance of Pd nanoparticles on titania nanotubes for the MOR. HR-TEM images revealed most of the nanotubes were close ended and multilayered with average outer and inner diameter of 15 and 10 nm, respectively. The interlayer spacing was found to be ~3 nm. Pd nanoparticles were deposited onto the titania nanotubes using the polyol process with $PdCl_2$ as the precursor and their performance towards methanol oxidation

was compared to that of Pd deposited on titania nanoparticles and pure Pd. 3 wt.% Pd–TiO_2 nanotubes displayed best current densities while 25 wt.% Pd performed the worst. Overall, the relative activities were Pd–TiO_2 nanotubes > Pd–TiO_2 particles > pure Pd [37]. Their study emphasised the role of the catalyst support on the performance of the catalyst and the effect of support morphology on the catalyst support interaction.

Many non-precious metals supported on titania have also demonstrated much improved ORR performance compared to the traditional Pt-based CB catalyst. Wu et al. synthesised Fe nanoparticles supported on polyaniline (PANI) treated TiO_2 nanoparticles and studied the samples for ORR activity. Commercial TiO_2 nanoparticles with particle size of 50–150 nm and surface area of 50–100 $m^2\,g^{-1}$ were first treated with 0.5 M HCl to remove any impurities. Aniline was polymerised in the presence of transition metal precursor ($FeCl_3$) and HCl treated TiO_2 nanoparticles were then added. The as-prepared catalysts were vacuum dried, ball milled and finally heat treated at 800–1000 °C in an inert atmosphere using N_2 gas. To remove any remaining unstable and inactive species, the catalysts were pre-leached in 0.5 M H_2SO_4 and then thoroughly washed in de-ionized water. SEM studies revealed that following polymerisation TiO_2 showed a transformation in morphology from nanoparticles to well dispersed nanofibre structures with a diameter of ~40 nm and length of ~200 nm. In order to explore the roles of nitrogen, iron and TiO_2 in ORR, the performance of the as-synthesized catalyst was compared to that of TiO_2, heat-treated PANI coated TiO_2 (PANI–TiO_2), and PANI–Fe supported on carbon black, Ketjen black EC-300J (PANI–Fe–C). Although TiO_2 has intrinsically low electronic activity, the PANI–Fe–TiO_2 electrocatalyst was found to be sufficiently conductive for operational use. This increase in conductivity was attributed to the formation of conductive graphitised carbon close to TiO_2 particles during PANI heat treatment resulting in 85 at.% carbon content. High performance durability was observed in PANI–Fe–TiO_2 during potential cycling in O_2 saturated electrolyte which showed a potential loss of only 12 mV after 5000 cycles compared to PANI–Fe–C (loss of ~80 mV). Comparable open circuit potential (OCP) values observed for PANI–Fe–C and PANI–Fe–TiO_2 in oxygen as well as air confirmed similar intrinsic activity of the two catalysts. FT-IR studies revealed graphitic nanofibre structure formation at 800 °C compared to non-heat treated PANI. The morphology became more porous at 900 °C showing much finer nanofibre structures. However, beyond 1000 °C the morphology became non-uniform resulting in large agglomerated particles. Another interesting observation reported was the presence of Ti–N due to possible substitution of O atoms with N atoms in TiO_2 crystal which was observed for PANI treated at 800 and 900 °C. The ORR performance for PANI–Fe–TiO_2 electrocatalyst was maximum after heat treatment at 900 °C. The improved performance was attributed to a number of reasons: (i) the presence of Ti–N–O/Ti–N–Ti structures as observed from XPS studies and (ii) presence of more anatase phase TiO_2 as observed from XRD analysis; aiding TiO_2 to promote ORR due to the increase electron conductivity and corrosion resistance [154].

3.1.2. Titanium nitride (TiN)

Another Ti based material studied in depth is TiN. This triple bond transition metal compound which is inert, has high mechanical hardness, high melting point and has high electrical conductivity (4000 S m^{-1} as opposed to 1190 S m^{-1} for carbon black) [155,156]. Its resistance to corrosion and high conductivity make it an excellent candidate for the synthesis of highly durable electrocatalysts and electrocatalyst support. Musthafa et al. used platinised TiN as electrocatalyst support system and found it to be extremely good for electrochemical oxidation of methanol with complete alleviation of CO poisoning effect. The reflectance infrared (IR) spectra of Pt–TiN before and after MOR identified a large increase in the –OH groups indicating Ti–OH formation which may help in alleviating CO poisoning effect similar to Ru–OH in Pt–Ru catalysts [38]. Avasarala et al. performed detailed durability and stability studies on TiN nanoparticles under fuel cell conditions. Commercial TiN nanoparticles with particle size of 20 nm and specific area of 40–55 $m^2\,g^{-1}$ were used as substrate to synthesis Pt nanoparticles using the polyol process. Behaviour of Pt/TiN was observed in sulphuric acid electrolyte at various operating temperatures. Active behaviour of Pt/TiN was observed for optimal conditions of 0.5 M H_2SO_4 and at 60 °C. Changes in the open circuit potential (OCP) of TiN nanoparticles were studied as a function of time at different temperatures in 0.5 M H_2SO_4. This revealed a downward shift in the OCP values (towards the active potentials) which was attributed to self activation of TiN indicating dissolution of oxynitrides on the surface of TiN and increased direct exposure of nitride surface to the acid solution. Faster oxynitride dissolution was observed when TiN was exposed to sulphuric acid at higher temperatures above 60 °C while low corrosion rate was observed in sulphuric acid at 60 °C. The decrease in OCP values was attributed to the formation of corrosion product on the nitride surface of TiN. Formation of positively charged corrosion products further led to adsorption of other negatively charges anions present in sulphuric acid. Consequently, the surface area of TiN nanoparticles is covered with a layer of oppositely charged ions prohibiting further dissolution of TiN and making the electrode passive. The authors studied the surface characteristics using XPS. Further studies to understand surface characteristics of TiN during active dissolution were performed by exposing TiN nanoparticles electrodes to *ideal* and extreme fuel cell conditions. Accelerated durability tests were performed on Pt/TiN in sulphuric and perchloric acid at 60 °C. The results were in agreement with the active/passive behaviour of TiN nanoparticles under electrochemical conditions [157].

3.1.3. Titanium diboride (TiB_2)

Titanium diboride is another relatively new titanium based support which has been investigated with a lot of interest. It is a ceramic with good electrical conductivity, thermal stability and corrosion resistance in acidic medium [158]. In 2010, for the first time, Yin et al. experimented with TiB_2 as a catalyst support material in PEMFC. In their studies, they observed that Pt/TiB_2 was found to be four times more electrochemically stable compared to commercial Pt/C under electrochemical oxidation cycles in the potential range +0.6 to +1.2 V *vs.* Hg/Hg_2SO_4. TiB_2 powders were prepared using a self-propagating high temperature synthesis while Pt nanoparticles were prepared using a colloidal route. During ultrasonic stirring of TiB_2 powders in ethanol, Pt colloid was added drop wise. A highly dispersed Pt loading of 18.6 wt.%, with an average Pt particle size of 3.4 nm, was obtained on TiB_2. TGA studies revealed that TiB_2 begins to oxidise as temperature approaches 532.2 °C. Cyclic voltammetry studies revealed no change in the redox region after oxidation for different durations implying no oxide formation on TiB_2 after 48 h at a potential hold at +1.2 V *vs.* Hg/Hg_2SO_4. Carbon black, on the other hand, suffered from surface oxide formation due to the hydroquinonequinone (HQ-Q) redox couple. Thus, TiB_2 showed better electrochemical stability compared to carbon black. The *ECSA* loss rate for Pt/TiB_2 was ~3.8 times slower than that of Pt/C and was attributed to the stability of TiB_2 and Nafion® acting as a stabilizer. The presence of $-SO_3$ groups in Nafion® allowed strong adhesion between the electron deficient TiB_2 surface and the electron rich $-SO_3$ groups in Nafion® making it the system act as a stabilizer [159].

3.1.4. Other dopants for titania

Other dopant metals that have been studied with titania include niobium (Nb) and ruthenium (Ru) [160]. Chhina et al. and Huang et al. reported the use of Pt supported on niobium-doped titania

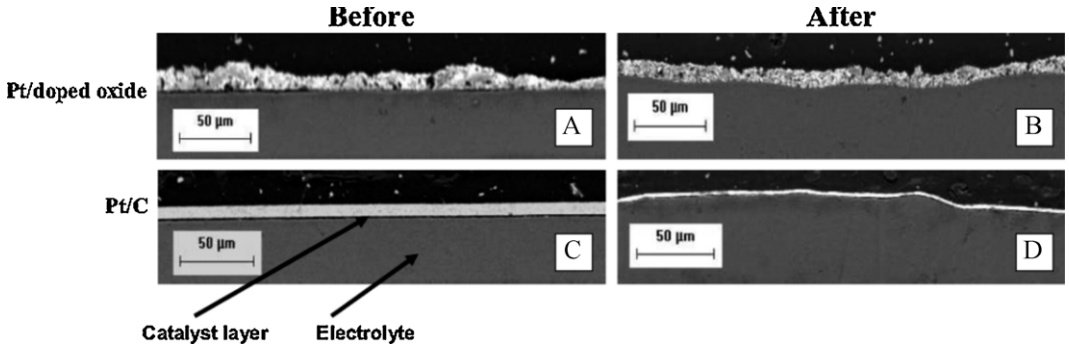

Fig. 9. SEM images of [A and B] 10 wt.% Pt/10Nb–TiO_2 and [C and D] HiSpec 4000 both before and after holding at +1.4 V for 20 h [161].

for PEMFCs [161,162]. Chhina et al. studied the stability of Nb–Ti catalyst support both *ex-situ* and *in-situ* in comparison to commercial Pt/C (JM HisSpec 4000). 10 mol% Nb-doped titania (Nb10–TiO_2) was prepared on which 10 wt.% Pt was deposited. Stability tests were performed by holding the cell voltage at +1.4 V for 20 h and polarisation curves were recorded before as well as after the potential hold. In fact, the authors reported that no change was observed in the Pt surface area for Nb10–TiO_2 support even after holding at +1.4 V for 60 h while a significant loss was observed for Pt/C. This observation was supported by TEM studies which showed no major change in catalyst morphology for Nb10–TiO_2 while significant catalyst agglomeration was observed for Pt/C after holding the cell voltage for 20 h. SEM micrographs (Fig. 9) also revealed a drop in catalyst thickness layer in Pt/C over no change in the case of Pt/Nb10–TiO_2 [161]. Huang et al. synthesised rutile phase Nb-doped titanium oxide and investigated its role as cathode catalyst support in PEMFC. Pt/$Nb_xTi_{(1-x)}O_2$ was prepared *via* a template assisted method in an ethanol medium and obtained in the form of a dark blue powder. TEM studied revealed 3–4 nm Pt nanoparticles, synthesised using the sodium borohydride reduction process, well-dispersed on Nb-Titania support. ORR activity was compared with commercial Pt/C (*E-TEK*). Half-cell ADT and ORR activity test performed using rotating ring disc electrode (RRDE) revealed minimum loss of Pt electrochemical active surface area for Pt/$Nb_xTi_{(1-x)}O_2$. Even after the potential test Pt/$Nb_xTi_{(1-x)}O_2$ showed a 10-fold increase in ORR activity compared to Pt/C. Furthermore, the Pt/C catalyst showed no activity in fuel cell testing after 1000 cycles. However, Pt/$Nb_xTi_{(1-x)}O_2$ catalyst showed only a small voltage loss (0.11 V at 0.6 A cm^{-2}) even after 3000 cycles [162].

Ru-doped titania supporting Pt nanoparticles were reported by Haas et al. and later by Wang et al. [39,40]. Haas et al. prepared $Ru_xTi_{1-x}O_2$ nanoparticles of various compositions by sol–gel methods. The as-prepared nanoparticles were ~200 nm in size. The mole fraction of Ru was varied in the range between 0.17 and 0.75. Pt loading varied from 27 wt.% to 40 wt.%. XRD studies identified the structure as rutile-type. All mixed oxides with a Ru mole fraction larger than 0.27 were found to be electronically conducting after 30 min of heat treatment at 450 °C. Cyclic voltammetry studies revealed that Pt supported on $Ru_xTi_{1-x}O_2$ displayed higher active surface area compared to CB. At RuO_2 concentration of $x_{Ru} = 0.71$, the Pt-surface area was determined to be nearly two times larger than the other oxide compositions and possessed higher specific area than pure Pt on Vulcan at the same Pt loading [39].

3.2. Tin oxide (SnO_2)

Tin oxide (SnO_2) is a transition-metal dioxide with rutile structures. It is usually regarded as oxygen deficient n-type semiconductor. Hydrous forms of SnO_2 appear to be hydrated particles of SnO_2 and are referred to as stannic acids. Chemical properties like adsorption of OH species at low potentials and ability to induce electronic effect with Pt have promoted SnO_2 as a potential fuel cell electrocatalyst support [36]. Studies conducted by Matsui et al. [274] revealed that when SnO_2 supported Pt catalysts were heat-treated at various temperatures under oxidizing or reducing atmospheres, their catalytic activity for electrochemical oxidation of CO were enhanced because of their peculiar microstructure and metal–support interactions. Okanishi et al. investigated the adsorption and catalytic properties of Pt/SnO_2 as a model system undergoing strong chemical interaction when subjected to oxidation–reduction treatments. Pt/SnO_2 was prepared using the impregnation method with Pt loading varying from 3 to 50 wt.%. In their work, very low CO adsorption was observed on the Pt/SnO_2 surface which had been pre-treated and reduced under hydrogen atmosphere at 400 °C. The reduced nanoparticles reportedly existed in a core-shell structure with Pt in the core enveloped in the oxide shell. The catalyst system was then used in a single cell PEMFC and its performance compared to that of Pt/C. Compared to that of Pt/C, no significant degradation of Pt/SnO_2 was reported on exposure to 100 ppm CO in the hydrogen stream. The study also identified that Pt/SnO_2 system was highly sensitive to the reduction–oxidation atmosphere and the surface reversibly between the two phases namely the metal–support and the intermetallic compound [41]. Masao et al. developed Pt supported on semi-conducting SnO_2 (Pt/SnO_2). Here, SnO_2 support was prepared using the co-precipitation method followed by calcination at 600 °C for 2 h. The Pt nanoparticles with a loading of 20 wt.% were prepared on SnO_2 *via* the colloidal method. The prepared SnO_2 support was thermodynamically stable The as-prepared Pt/SnO_2 were heat treated at different temperatures in 5% H_2–N_2 atmosphere leading to the co-existence of metallic Pt and SnO_2 as separate phases. Pt nanoparticles of average diameter ~3 nm, homogeneously distributed on SnO_2 nanoparticles with average diameter of several tens of nanometers, were observed in TEM images. It was also reported that Pt/SnO_2 electrocatlysts exhibited significant tolerance against potential cycling up to +1.3 V *vs.* RHE even after 10,000 cycles [163]. Zhang et al. prepared oxidation resistant, high surface area (205 m^2 g^{-1}) mesoporous SnO_2 with narrow pore size distribution. In this investigation, mesoporous SnO_2 was prepared using neutral surfactant template-assisted method. A modified polyol process was used to deposit Pt nanoparticles on mesoporous SnO_2. XRD measurements showed that SnO_2 nanoparticles and Pt nanoparticles had an average size of 6.1 and 5.2 nm, respectively. The performance of Pt/SnO_2 system was compared to that of commercial Pt/C (Vulcan XC-71 and Ketjen Black EC 300J) and electrochemical stability and durability were investigated using accelerated stress tests. The authors repeated the potential cycling tests at different cell temperatures and compared the normalised *ECSA* for the different samples (Fig. 10). These along with the EIS

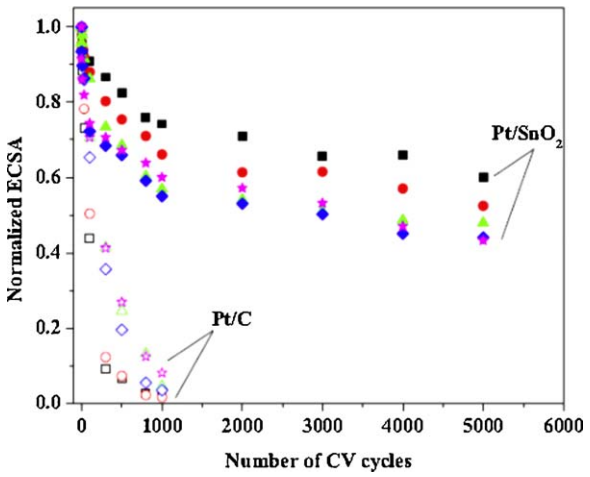

Fig. 10. Normalized *ECSA* as a function of CV cycling numbers for the Pt/C and Pt/SnO_2 catalysts at 70 °C (square), 75 °C (circle), 80 °C (triangle), 85 °C (star), and 90 °C (diamond) [164].

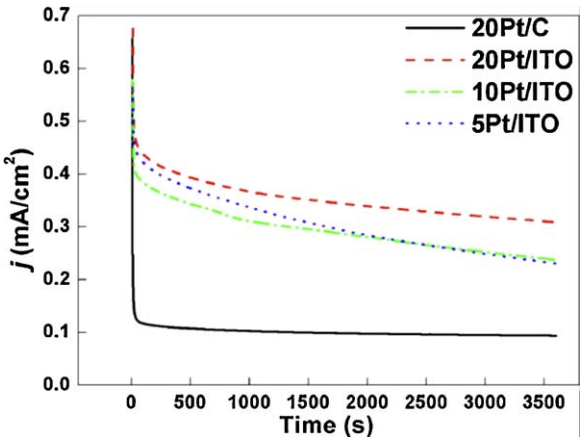

Fig. 11. Current–time curve of the ITO supported Pt catalysts and carbon-supported Pt catalyst (20 wt.% Pt on CB) [173].

studies revealed similar electrochemical activity but significantly improved electrochemical stability of Pt/SnO_2 compared to that of commercial Pt/C especially at high potentials [164].

However, some issues regarding instability of SnO_2 under electrochemical conditions still persist; as such it is often doped or alloyed with other metals such as antimony, ruthenium, indium, etc. to improve its stability [165–169]. Lee et al. reported studies conducted on Pt deposited on antimony doped tin oxide (Pt/ATO) to examine the electrochemical activity and stability for the methanol and ethanol oxidation reactions. For comparison purposes, CV and chronoamperometry (CA) studies were performed using commercial Pt/C with Pt loading of 40 wt.%. Different Pt loading were also prepared on ATO based on the polyol method. XRD studies identified average ATO nanoparticle size of 5.2 nm while the BET surface area was observed as 99.7 $m^2\,g^{-1}$ which was much lower than the value for Vulcan XC-72 (239.6 $m^2\,g^{-1}$). TEM studies performed on the Pt/ATO samples revealed that the average Pt particle size was ~2.5 nm with good dispersion of Pt nanoparticles on the ATO support. CO-stripping experiments showed that Pt/ATO to be highly CO-tolerant. It was also observed that Pt/ATO was more effective than Pt/C for the electro-oxidation of both weakly and strongly adsorbed CO along with more negative CO oxidation potential compared to Pt/C. The high electrochemical stability of Pt/ATO was attributed to the rough surface of oxide support which led to stronger interaction with the catalyst and higher corrosion resistance of the ATO support. The ethanol oxidation reactivity (EOR), for Pt/ATO was found to be much enhanced compared to Pt/C than the MOR [167]. Pang et al. synthesised Ru doped SnO_2 nanoparticles supported Pt. Ru-doped SnO_2 was synthesised using chemical precipitation and calcination. These were tested as catalyst support as well as second catalyst (forming binary system with Pt) for the MOR. The authors studied the morphology, composition the as-synthesis SnO_2 and Ru doped SnO_2 particles using SEM, EDX and XRD analysis. Impedance spectroscopy (EIS) studies revealed Ru doping enhanced the conductivity of SnO_2 proving beneficial for the methanol electro-oxidation. Although no electrocatalytic activity was observed for Ru-doped SnO_2 nanoparticles towards the MOR, the methanol oxidation peak current for Pt/Ru-doped SnO_2 was found to be 3.56 times higher than that of the Pt/SnO_2 electrocatalyst. Tafel plot studies indicated that the Ru-doped SnO_2 significantly improved the kinetics for MOR. The optimal atomic ratio of Ru to Sn in Pt/Ru-doped SnO_2 was found to be 1:75 which displayed 6.75 times higher electrochemical activity as well as long term cycle stability compared to Pt/SnO_2 [169].

3.3. Indium tin oxide (ITO)

Indium oxide In_2O_3 is a crystalline structure. It was shown that the substitutional doping of In_2O_3 involving the replacement of In^{3+} atoms with Sn^{4+} in the cubic bixbyite structure enhances the conductivity to values $>10^3$ S cm^{-1} and also affects the optical properties generating ITO films [170,171b]. ITO has been long used as a transparent conducting material for liquid crystal display applications [172]. Chhina et al. investigated the use of ITO as a catalyst support for fuel cell applications for the first time. In their studies, Pt (40 wt.%) was dispersed on commercially available ITO by reflux method. The thermal and electrochemical stability of Pt/ITO was compared with that of (i) commercially available 40 wt.% Pt deposited on Vulcan XC-72R (JM Hispec 4000) and (ii) 40 wt.% Pt dispersed on Vulcan XC-72R, produced *in-house*. The XRD characterisation revealed an average crystallite size of 13 nm and 38 nm for Pt and ITO respectively and the TEM and SEM images showed Pt clusters dispersed on small octahedral shaped crystalline ITO particles. Cyclic voltammetry studies revealed that the Pt/ITO to be much more stable electrochemically. Both the Pt/C catalyst samples showed significant loss of active surface area due to continuous cycling. Thermal stability studies were conducted using TGA and it was found that Pt/ITO was extremely stable (~1 wt.% loss) compared to the Pt/C JM Hispec 4000 samples (57 wt.% loss) when heated to 1000 °C in air [42]. Park et al. deposited preformed colloidal Pt nanoparticles onto ITO nanoparticles synthesised *in-house* using the glycine nitrate process. XRD profiles along with EDX and SEM revealed ITO crystallite size of 26 nm with Sn well incorporated into In_2O_3 lattice formed the support for Pt nanoparticles. Pt nanoparticles dispersed on ITO as observed from TEM were ~4 nm in size. High intrinsic activity was observed for Pt/ITO during methanol electro-oxidation when compared to commercial Pt/C. Relatively high stability (chronoamperometry curves shown in Fig. 11) was also observed during potential cycling despite larger particle size of ITO and lower *ECSA* values. Electrochemical impedance studies found ITO supported Pt exhibited a faster electron kinetics or lower charge transfer resistance which decreased with the decrease in the metal loading. CO striping experiments revealed that lower onset and peak potentials of Pt/ITO samples were obtained indicating that adsorbed CO was oxidised at a lower potential for ITO supported Pt. The high catalytic activity was attributed to the active participation of ITO in the methanol oxidation process. It was suggested that interaction of SnO_2 or In_2O_3 phase of ITO with the adsorbed intermediate CO on Pt could provide oxygen species at lower potentials [173]. Some unconventional catalyst architectures supported on ITO have also been explored.

For example, Zhang et al. formed a facile template free method to grow Pt nanoflower structures on ITO substrates. Their experiments revealed that the Pt nanoflower structure on ITO exhibited remarkably high catalytic activity and stronger tolerance to poisoning for methanol oxidation when compared to conventional Pt nanoparticles on ITO substrates [174].

Bimetallic nanoparticles–ITO systems have also been investigated. Song et al. successfully prepared Au–Pt hybrid nanoparticles on ITO surface using a direct electrodeposition method. The method revealed that the size of the Au nanoparticles could be controlled by the number of electrodeposition cycles. SEM and XRD studies found the 'cauliflower' shaped Au–Pt nanoparticles with average diameter of ~60 nm were deposited onto ITO. The as-prepared Au–Pt/ITO electrodes not only exhibited lower charge transfer resistance upon the deposition of noble and bimetallic nanoparticles on ITO but also demonstrated electrocatalytic activity towards ORR [175].

3.4. Silicon dioxide (SiO_2)

Silicon dioxide or silica is well known for its hardness and exists in various crystalline as well as amorphous forms. Most of its crystalline forms consist of tetrahedral SiO_4 units. Silica was initially introduced to fuel cells as an essential component of preparation of self-humidifying membranes. Wang et al. and Zhu et al. reported in 2006 the use of silica in preparation of self-humidifying polymer membranes (Pt/SiO_2 modified Nafion®/PTFE) for applications in fuel cells [176,177]. The Pt/SiO_2 nanoparticles catalysed the recombination of H_2 and O_2 and the SiO_2 nanoparticles were able to absorb the water produced at Pt/SiO_2. Thus hydrophilic Pt/SiO_2 nanoparticles enabled the membranes to minimise conductivity loss under dry conditions.

More recently, the use of silica as support material for Pt electrocatalyst at the cathode has been explored by Seger et al. [43]. They prepared Pt nanoparticles on a colloidal silica substrate by reduction using sodium borohydride. Controlling the Pt–SiO_2 ratio enabled them to obtain well-dispersed catalyst surface with minimal conductivity loss. TEM images revealed that lower concentrations of Pt allowed uniform Pt dispersions with interconnected particle-network enabling higher conductivity and higher surface area. The average size of the SiO_2 core was found to be 4 nm. The as-prepared SiO_2–Pt core-shell particle structure was studied as cathode catalyst in an MEA. The authors compared the performance of Pt/SiO_2 to that of commercial *E-TEK* which revealed higher electrocatalytic active area, and much improved charge transfer kinetics for Pt–SiO_2. Best power densities were reported for the sample with Pt:SiO_2 ratio of 2:1. Similar ohmic losses were observed in current interrupt (CI) tests for both Pt/SiO_2 and *E-TEK* samples confirming no contribution of silica to the overall resistivity.

Wang et al. produced Pt electrocatalyst supported on carbon nitride modified SiO_2 ($Pt/CN_x/SiO_2$) for ORR [178]. The CN_x/SiO_2 composite was produced by *in-situ* polymerisation method using calcination of polypyrrole coated SiO_2 at 800 °C. Pt nanoparticles were deposited using polyol process. Comparison studies were performed using $Pt/CN_x/C$ electrocatalyst prepared from commercial Pt/C using the same synthesis technique and same Pt loading. BET measurements identified surface area of CN_x/SiO_2 as 258 $m^2\,g^{-1}$, which was slightly higher than that measured for Vulcan XC-72, i.e. 245 $m^2\,g^{-1}$. XRD measurements revealed Pt particle sizes of ~4.3, ~4.1 and ~4.0 nm for Pt/C, $Pt/CN_x/C$ and $Pt/CN_x/SiO_2$, respectively. The *ESCA* value for $Pt/CN_x/SiO_2$ was reported to be 89.6 $m^2\,g^{-1}$, which is much higher than the values reported in literature for Pt/C and $Pt/CN_x/C$. Mass activity for $Pt/CN_x/SiO_2$ was found to be 1.52 and 1.59 times higher than that of Pt/C and 1.31 and 1.32 times higher than that of $Pt/CN_x/C$ electrocatalyst at +0.85 and +0.80 V *vs.* RHE, respectively. It was further observed that CN_x/SiO_2 supported catalyst exhibited much higher durability towards the ORR. The improved activity, durability and performance of the CN_x/SiO_2 supported catalyst was attributed to the presence of (i) SiO_2 species which exhibited Ru like oxophilic behaviour and (ii) N species encouraging a synergistic effect between the catalyst and the support.

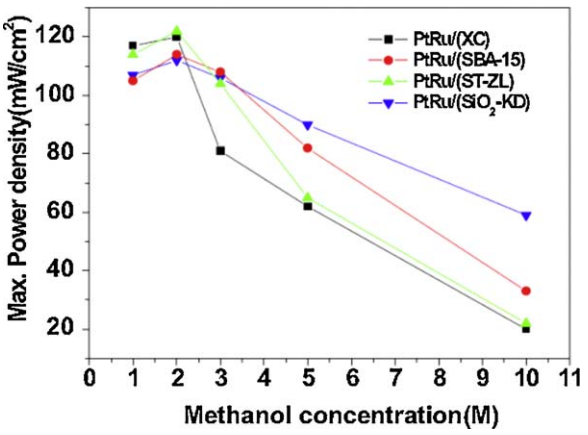

Fig. 12. Performance results with various catalysts namely, SBA-15, ST-ZL (Snowtex), homemade silica (SiO_2-KD, and carbon black powder (Vulcan XC-72R, Cabot, XC) at different methanol concentrations [179].

Nam et al. recently reported investigations of Pt–Ru supported on silica as anode for DMFC using a range of methanol concentrations (from 1 to 10 M) through single cell tests. The silica-supported Pt–Ru catalysts exhibited higher performance in MEA, with the maximum power density reaching up to 90 mW cm^{-2} and 60 mW cm^{-2} at 5 M and 10 M methanol concentration, respectively (Fig. 12). This was up to 3 times higher than the performance of CB supported catalyst [179].

3.5. Tungsten (W)

Tungsten is a versatile transition element which is capable of forming a variety of oxides (from −1 to +6) and carbides. The existence of various oxidation states makes tungsten suitable for a variety of photochromic, electrochromic, photocatalytic, gas-sensor and fuel cell applications [180,181].

3.5.1. Tungsten oxide (WO_x)

Tungsten oxide is an n-type semi-conductor with a band gap of 2.6–2.8 eV [182]. Pt and its other alloy catalyst nanoparticles deposited on tungsten oxide substrates are reported to display much higher electrocatalytic activity. These materials are also strongly resistant to corrosion. Tungsten oxide supported Pt electrocatalysts also show much enhanced CO tolerance during MOR and ORR. The resistance of tungsten oxides towards CO poisoning during catalytic oxidation in fuel cells was first reported by Niedrach et al. in 1969 [183]. This was followed by the work of Kulesza and Faulkner who reported that Pt dispersed on WO exhibited enhanced electrocatalytic activity towards MOR [44,45]. It has been clearly demonstrated in the works of Li et al. and also in the studies conducted by Nakajima et al. that tungsten oxides tend to form tungsten trioxide hydrates which enable enhanced proton transfer similar to that in case of titanium oxides. This mechanism has also been verified for Pt–Ru–WO_3 catalyst–support systems [184,185].

Tungsten oxides are also being used as anode and cathode electrocatalysts, co-catalysts and even electrolytes in various fuel cells including DMFC. Antolini and Gonzalez have published a detailed review on the use of tungsten based materials in various aspects of fuel cells and the readers are invited to explore it [186].

Chhina et al. performed detailed studies on the oxidative stability of commercial tungsten oxide by applying accelerated oxidation cycles at room temperature and compared it to the stability of carbon catalyst support. They also studied the activity of Pt dispersed on tungsten oxide support both at room temperature and at 80 °C. They used an alternative method for the deposition of Pt nanoaprticles on tungsten oxide. The method involved addition of tungsten oxide into sulphuric acid. The solution temperature was increased to 75 °C and chloroplatinic acid was added to this in the presence of hydrogen. This resulted in reduction of Pt onto tungsten oxide. The CV results for 40 wt.% Pt/WO compared to those of JM Hispec 4000 (40 wt.% Pt/C) showed that Pt/WO is stable even after 100 oxidation cycles, while JM Hispec 4000 lost its entire Pt oxide reduction peak area (∼+0.75 V *vs.* RHE) after only 10 oxidation cycles. The authors also studied the Tafel plots of the ORR activity both before and after oxidation cycles at 80 °C for 40 wt.% Pt/WO and compared these to JM Hispec 4000. They observed significantly greater stability and higher catalyst activity of the Pt/WO catalyst, as observed by after oxidation cycles for Pt/WO. However, the overall catalytic activity of the Pt/WO catalyst was reported to be lower than that of the JM Hispec 4000. This was attributed to: (i) lower surface area of the commercial tungsten oxide compared to the high-surface-area-based catalyst support (250 $m^2\ g^{-1}$) used for JM Hispec 4000; (ii) lower conductivity of tungsten oxide compared to CB and (iii) the use of chloroplatinic acid which is reduced to Pt metal even in the absence of tungsten oxide, which could lead to some Pt clusters that are not supported on tungsten oxide and may not be connected to a conduction pathway, thus further decreasing catalyst activity for a given Pt loading. The authors also suggested that the use of doped tungsten oxide for increasing the conductivity of tungsten oxide and other synthesis routes such as sol–gel methods which can provide high-surface-area tungsten oxide and improve catalytic activity [181].

Although various techniques like co-electrodeposition [187], co-sputtering [188,189] freeze-drying [190,191] and the sol–gel [192,193] have been explored for the Pt/WO_x synthesis, it was found that the sol–gel approach provides several benefits including greater surface area, ease of preparation and smaller particle size. Mcleod et al. synthesised WO_x by means of two different methods (using ethanol and water based solvents) using the sol–gel approach with $W(OC_2H_5)_6$ as the precursor. Pt sol was prepared using a solution of $NaOC_2H_5$ and H_2PtCl_6 which was refluxed in absolute ethanol under Ar for 2 h. Pt solution was then combined with the WO_x solutions. The colour change in the WO_x films from initial dark brown to orange to white after drying indicated the oxidation from of W(V) to W(VI) which is active for co-catalysis and support purposes. In this work, several WO_x:Pt ratios were studied. Electrochemical studies showed that the characteristic shape of the cyclic voltammograms and the *electrochromic* behaviour of both types of WO_x films exhibited a rapid intercalation/de-intercalation of protons and electrons during the W(V) oxide/W(VI) oxide redox reactions. It was observed that the WO_x films prepared in aqueous media as opposed to those in ethanol, exhibited more stable methanol oxidation with a clear evidence of co-catalysis. In the case of water based WO_x, films with WO_x:Pt ratio higher than 3 showed very slow decay in methanol oxidation current. However, a maximum current decay was observed for WO_x:Pt ratio of 5 which was attributed to a change in film morphology at this ratio. The change in the film morphology was also confirmed in SEM and resulted in a more open structure that allowed better penetration of the methanol solution into the film [193]. Micoud et al. performed studies to understand the effect of WO_x support in the electro-oxidation of a monolayer of CO_{ads} using Pt catalyst. The performance was compared to that of Pt/C. Monoclinic WO_3 nanoparticles (8 $m^2\ g^{-1}$) were loaded with 7 wt.% Pt nanoparticles. Pt nanoparticles with average mean diameter of 2.7 nm were homogeneously distributed over WO_3 with very less agglomeration. Ar purged and H_2 purged CO_{ads} stripping experiments were performed which revealed that the number of active sites were limited. When H_2 was purged to liberate the electrolyte from CO, a steep and continuous increase of the H_2 electro-oxidation current was observed. This indicated towards continuous liberation of the Pt catalytic sites from the adsorbed species. Pt/WO_x were found to demonstrate high tolerance towards CO which was attributed to a strong metal–support interaction (SMSI), involving the formation of a metal-oxide film partially covering or encapsulating the Pt nanoparticles as well as to the formation of W–OH groups upon H^+ insertion at low electrode potentials [194].

Different morphologies of tungsten oxide like microsphere and nanowires have also been investigated with great interest as catalyst support in DMFC and PEMFC [49,195]. Ganesan et al. synthesized tungsten trioxide microspheres by the oxidation of tungsten carbide (WC). Performance of Pt nanoparticles (∼6.5 nm) supported on WO_x microspheres was compared with commercial 20 wt.% Pt–Ru/Vulcan-XC72 carbon and 20 wt.% Pt–Ru/carbon microspheres. Pt/WO_x microspheres demonstrated very high activity towards the MOR which exceeded that of Pt–Ru catalyst supported on carbon microspheres as well as commercial Pt–Ru catalysts with a higher metal loading. CV studies performed on tungsten trioxide microspheres indicated that these microspheres were stable and did not undergo any dissolution in acid medium. For the MOR studies, the methanol oxidation onset potential and anodic peak potential of Pt/WO_3 was found to be 100 and 50 mV more negative than that of the commercial *E-Tek* catalyst, respectively. This was attributed to better CO tolerance of the catalyst. A decrease in the peak-to-peak separation of the forward and the backward scans was also observed, i.e. ΔE_p = +80 mV for Pt/WO_3, ΔE_p = +270 mV for commercial *E-Tek* catalyst and ΔE_p = +210 mV for Pt–Ru/C. This further confirmed that Pt/WO_3 catalyst has greater tolerance towards CO [49]. Saha et al. studied carbon coated tungsten oxide nanowires for the ORR as cathode catalyst supports. The nanowires were grown on carbon fibre of carbon paper (C–$W_{18}O_{49}$ NWs/carbon paper) using chemical vapour deposition. Pt nanoparticles were deposited on the nanowires using glacial acetic acid as the reducing agent for the Pt precursor. SEM and TEM images (Fig. 13) revealed Pt nanoparticles of 1–3 nm diameter (average 2.27 nm) deposited on nanowires with diameter ranging from 30 to 60 nm. CV studies revealed that the Pt/C–$W_{18}O_{49}$ NWs/carbon paper composite had a mass specific surface area of ca. 36% higher and a roughness factor about 30% higher than that of the commercial Pt/C electrode. A +100 mV potential shift was also observed in the onset potential for the ORR at the Pt/C–$W_{18}O_{49}$ NWs/carbon paper composite electrode as compared to Pt/C. The nanowire composite also showed higher ORR current and 75% higher mass activity than that of commercial Pt/C [195].

Although studies conducted on oxides have reported encouraging performance displayed by various oxides as catalyst–support for fuel cell. However, problems like low surface area and low conductivity are commonly observed for most oxides. Moreover, some oxides are also unstable in acidic environments. Since their properties are largely dependent on composition and structure, these offer a range of challenges for researchers to explore suitable materials.

3.5.2. Tungsten carbide (WC)

Tungsten carbide is one of the hardest known carbides, is resistant to chemical attack and behaves similar to unalloyed tungsten. However, on exposure to air surface oxidation occurs which increases with time while on exposure to water it undergoes continuous oxidation and dissolution. The surface oxidation preferentially progresses on sites where the oxide species are already in existence. This leads to a simultaneous oxidation of tungsten and carbon [196,186]. It is well known that near the *Fermi* level, the

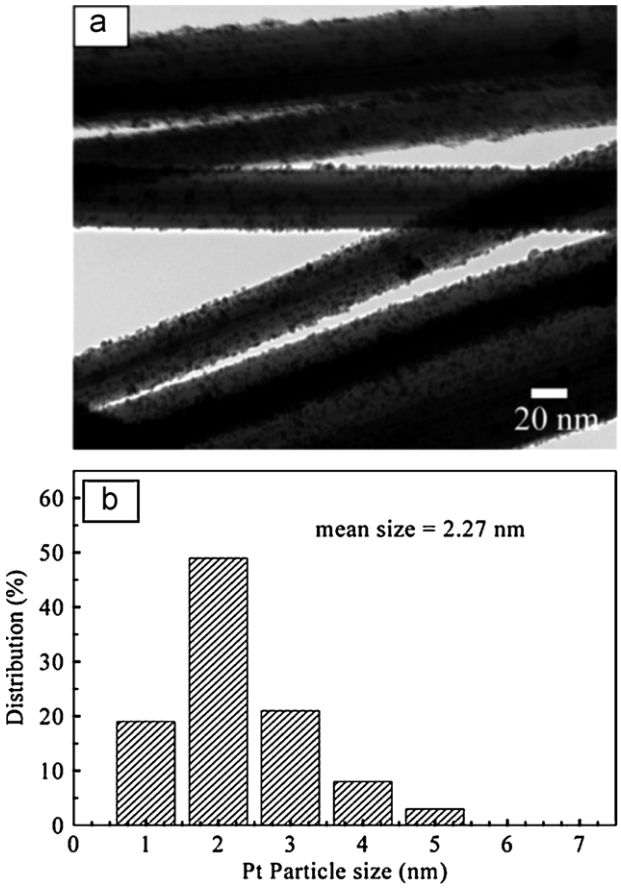

Fig. 13. (a) TEM images of Pt nanoparticles deposited on the C-$W_{18}O_{49}$ NWs/carbon paper by glacial acetic acid method and (b) the corresponding particle size distribution [195].

electronic states of tungsten carbide resemble those of platinum metal, in its noble form [197]. In fact, due to the similarity of their electronic states with noble Pt at the *Fermi* level, carbides of tungsten have been studied as catalysts supports, co-catalysts, as well as electrocatalysts [46–50]. Tungsten carbides, similar to its oxides, enhance the electrocatalyst CO tolerance during methanol oxidation. They also promote ORR at the cathode [50]. The commonly used and most important tungsten carbides are WC and W_2C. While WC is a stable compound, W_2C is known to be thermodynamically unstable at low temperatures. WC also exhibits very high durability under fuel cell conditions. This was experimentally confirmed in the studies of Zellner et al. who conducted electrochemical CV measurements and XPS analysis. The authors concluded that WC remained stable at anode potentials of 0.6 V *vs.* SHE in 0.5 M H_2SO_4 solution [198].

Some studies conducted by Shen, Meng and co-workers revealed enhanced catalytic activities for electrocatalyst other than Pt (like Pt, Au, Pd and Ag nanoparticles) supported on WC. It was observed that CO is much easily oxidised on the surface of WC and Pt/WC compared to that of Pt which consequently lowers the onset potentials for CO oxidation in the presence of WC as catalyst or support [199,200]. Bosco et al. Prepared three-dimensionally ordered macroporous tungsten carbide (3DOM WC) with varying pore size using the "inverse-opal" method [47] More recently Cui et al. and Fu et al. have performed in-depth studies on WC supports for Pt which exhibited enhanced 'anti-poisoning' behaviour for methanol oxidation as compared to Pt/C catalysts. They prepared Pt–WC/C by depositing Pt on WC support using intermittent microwave heating. A negative shift was observed in the onset potential for methanol oxidation along with an increased anodic peak current density. CO stripping experiments suggested that the adsorbed CO was oxidised and removed much more easily from the Pt–WC/C surface compared to that of Pt/C. Their results were further supported by density functional theory (DFT) and the theoretical surface electrostatic potential calculations which suggested that WC support could provide a stronger negative electronic property to Pt atoms through an electron donating effect. The authors suggested that the electron donation would be beneficial for avoiding CO adsorption as well as promoting the oxidation of any adsorbed CO [50]. Fu et al. prepared mesoporous tungsten carbide (WC) supported Pt nanoparticles. In their work, the mesoporous WC (*m*-WC) was synthesized by evaporation-induced triconstituent co-assembly method. The samples were then carburised at various temperatures in the range 600–1000 °C for 3 h. Pt nanoparticles were then deposited onto *m*-WC using the sodium borohydride reduction method. TEM images revealed Pt nanoparticle size of ~10 nm while *m*-WC had a porous structure with diameter of ~4 nm. BET studies revealed highest specific surface area (182 $m^2\ g^{-1}$) for *m*-WC carburised at 900 °C. The samples also had narrower pore size distribution of ~3.9 nm. CV, CA (Fig. 14) and CO-stripping studies were performed to compare the performance of Pt/*m*-WC with that of Pt/C. Pt/*m*-WC samples showed higher electrocatalytic activity, along with much higher CO tolerance and stability [201].

Zhou et al. reported the synthesis of Pt supported on WC nanofibres with ultrathin diameters. The nanofibres were produced using carbon spinning technique followed by carbonisation at high temperature using ammonium metatungstate (AMT) and polyvinyl pyrrolidone (PVP) as precursor fibres. RDE and Koutecky–Levich (K–L) plots revealed that the ORR process mainly favoured the four-electron pathway over WC (NH_3, 850 °C), while a two-electron pathway was favoured over WC (pristine). Electrocatalytic stabilities of WC (pristine) and WC (NH_3, 850 °C) were measured at −0.40 V *vs.* Ag/AgCl for 20,000 s in O_2-saturated 0.1 M KOH solution at a rotating rate of 1600 rpm. It was observed that the ORR current of the pristine WC nanofibres decreased significantly by ca. 15% after 20,000 s compared to 7.5% decrease for the WC (NH_3, 850 °C) [202].

In summary, the studies on carbides reveal that there are still potential challenges such as achieving optimal Pt particle size and better catalyst dispersion on these carbide structures, which need to be addressed.

3.6. Sulfated zirconia (SZ)

The surface of zirconia or zirconium oxide is known to possess oxidation and reduction properties. Upon modification with sulphate ions it forms a highly acidic or super-acidic catalyst, sulphated zirconia (S-ZrO_2). Hence, sulphated zirconia (SZ) exhibits superior catalytic activities for various reactions of industrial importance. S-ZrO_2 has a *Hammet* acid strength higher than that of 100% sulphuric acid. It is highly hydrophilic, possesses high proton conductivity and retains high catalytic activity in the presence of methanol and water even at temperatures up to 300 °C [203,204].

Suzuki et al. synthesised sulphated zirconia supported Pt which were studied as cathode electrocatalyst for PEMFC. The cathode electrocatalyst was prepared using commercially available S-ZrO_2 with a surface area 80 $m^2\ g^{-1}$, on which Pt nanoparticles were dispersed *via* ultrasonic spray pyrolysis. MEA were prepared using Pt/S-ZrO_2 with and without Nafion® and the performance was compared with that of commercial Pt/C (Tanaka TKK 46 wt.% Pt). SEM, TEM and XRD studies revealed well dispersed Pt nanoparticles (~8 nm) on the surface of S-ZrO_2 particles of ~50–100 nm. The presence of SO_x groups during TGA studies confirmed their stability on ZrO_2 surface as they remained on the surface even after pyrolysis

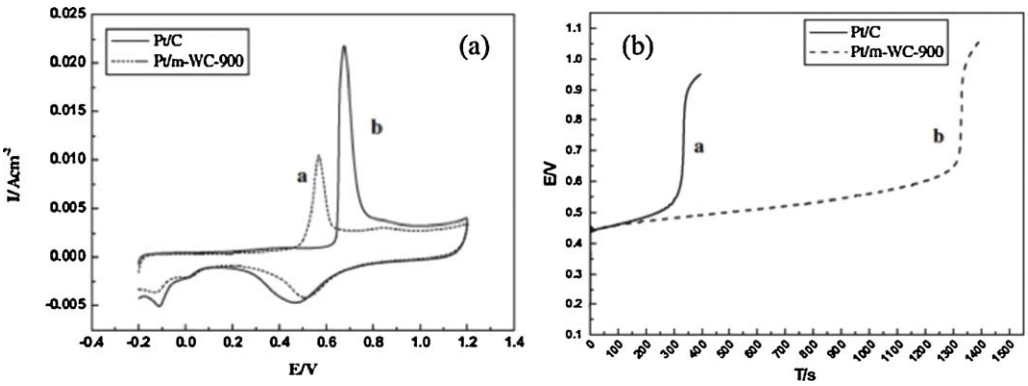

Fig. 14. (a) Cyclic voltammograms of Pt/m-WC-900 and Pt/C after CO adsorption in 0.5 M H_2SO_4 solution. Scan rate: 50 mV s^{-1}. (b) Chronopotentiometric curves of Pt/C and Pt/m-WC-900 in 0.5 M H_2SO_4 + 0.5 M CH_3OH [201].

at 650 °C. The fuel cell performance of Pt/S-ZrO_2 with Nafion® was found to be lower than that of Pt/C with Nafion®; while Pt/S-ZrO_2 without Nafion® displayed better performance compared to Pt/C without Nafion®. Although the fuel cell performance decreased for both cathodes in the absence of Nafion®, the ratio (with Nafion® ionomer: without Nafion® ionomer) of the cell voltage decrease for Pt/S–ZrO_2 was 16% compared to ~33% for Pt/C [51].

Sulphated zirconia nanoparticles are also used for effective proton conduction [204,205]. In 2004 Hara and Miyayama studied the proton conductivity of sulphated zirconia for the first time by preparing sulphated zirconia with hydrated zirconia and sulphuric acid using several methods. They found that (i) SZ displayed high conductivity of the order of 10^{-2} S m^{-1} and (ii) the S/Zr ratio affected the conductivity of SZ and higher ratio led to higher conductivity. The high proton conductivity was attributed to the localised electrons on O in SO_x species and the *Lewis acid* points on Zr which can easily generate new *Brønsted acid* points leading to higher conductivity [204]. Later, Tominaka et al. produced sulphated zirconia nanoparticles using two different methods: (i) conventional method, i.e. using solvent (S-SZ) and (ii) using solvent-free synthesis (SF-SZ). The TEM studies revealed that S-SZ and SF-SZ particles displayed an average size of 50–100 nm and 5–10 nm, respectively. While S-SZ showed a mixed crystalline form consisting of monoclinic and tetragonal phase of zirconia; SF-SZ was found to be completely amorphous which is unusual for sulphated zirconia. The presence of amorphous structures indicated smaller particle size which was confirmed by TEM studies. The sulphur content of SF-SZ was about three times higher than that of S-SZ from the EDXS studies while no precursor residues were detected in the TGA studies. SF-SZ also displayed high ionic conductivity (10^{-2} S m^{-1}) which is comparable to that of Nafion® [205]. Due to its high proton conductivity and high catalytic activity even at high temperatures, it is also being used to modify proton exchange membranes such as Nafion®.

4. Conducting polymers

The use of conducting polymers as catalyst supports for metal nanoparticles was first attempted by Pickup and group using electronically and ionically conducting polypyrrole/polystyrene-sulfonate particles as support for Pt and Pt oxide nanoparticles [206]. Later, other conducting polymers and their composites such as poly(3,4-ethylenedioxythiophene)–poly(styrene sulfonic acid) or PEDOT-PSS [207–209]; PEDOT [208,210,211]; poly(N-vinyl carbazole), poly(9-(4-vinylphenyl) carbazole) [212]; polyaniline (PANI), Nafion® [213]; poly(diallyldimethylammonium chloride) or PDDA [214]; and poly(N-acteylaniline) [215] have shown quite promising results. Spătaru et al. investigated the use of polytertamine (PTy) as an alternative conducting membrane to act as catalyst support [216]. Tyramine belongs to the class of monomers that contain aromatic groups directly linked to oxygen which readily encourages polymersation, enabling polymer coatings with higher electrochemical and mechanical stability. In addition, tyramine (Ty) (4-(2-aminoethyl) phenol) has a free amine group which allows to purposefully modify it by covalent attachment of various molecules [217,218]. In the studies conducted by Spătaru et al., polytyramine films were grown and deposited onto graphite substrate *via* potentiodynamic electropolymerisation (schematic

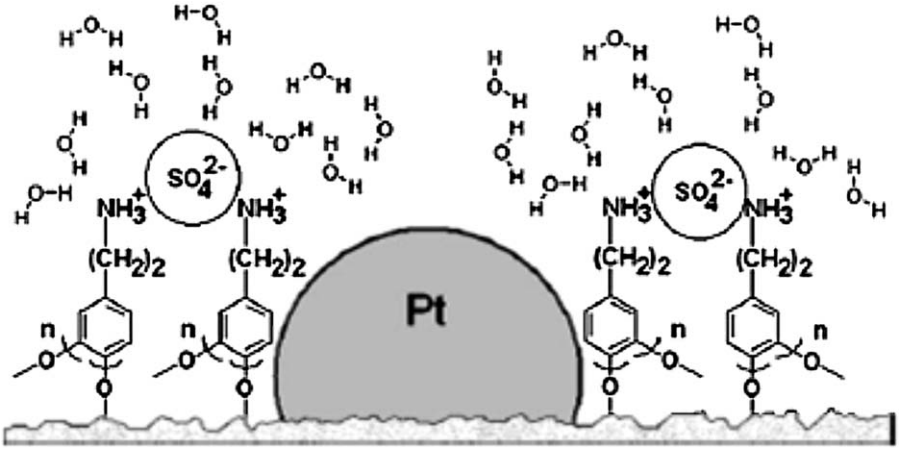

Fig. 15. Schematic tentatively explaining the role of the amine groups from the PTy in promoting the formation of Pt–OH species [216].

Table 1
Types of carbonaceous support materials: properties, catalysts and observations.

Type of support	Support properties	Catalysts (particle size); loading	ECSA ($m^2\ g^{-1}$)	Power density ($mW\ cm^{-2}$)	Electrode	Observation/comments	Ref.
CNT (SWCNT, MWCNT)	• sp^2 carbon • Hydrophobic • High conductivity • N-doped CNTs for ORR	Pt (2–5 nm) 0.04 mg cm^{-2}, Pt–Ru (3–4 nm) 2.5 mg cm^{-2}; Pt–Co (5–10 nm), Pt–Fe, Pt–Ni, Pt–WO_3; Pt–Ru–Ir, Pt–Ru–Ni, Ru–Se, etc. Mono, binary and tertiary alloys	Upto 44.3 (anode)	39.3–62 (anode) 595 (cathode)	Anode, cathode	• Larger catalyst particles without surface treatment • Good metal dispersion in case of SWCNT • High metal stability for MWCNT	[230] [77b] [25] [75] [76] [77]
CNF	• sp^2 carbon • High conductivity • 3.9 S cm^{-1} • High durability • N-doping for ORR	Pt (3–8 nm, recently, <5 nm), Pt–Ru (<5 nm)	20–80	93 (anode) 900 (cathode)	Anode, cathode	• Long term stability and durability • Increased graphitisation enhances ORR	[93] [94] [97] [231]
OMC, DOMC	• sp^2/sp^3 carbon • High SA • 0.3 S cm^{-1} • Good pore structure and size distribution • Few O-functional groups	Pt (0.5 mg cm^{-2}) <8 nm Pt–Ru, Fe 2 mg cm^{-2}	62.96–208.2 ~28 μg cm^{-2}	80 (anode)–500 (cathode)	Anode, cathode	• Easier mass transportation with desired pore morphology • Lack of good contact between Pt and Nafion buried inside large pore DOMC	[32] [107] [108] [232] [233] [234] [235] [236] [104]
ND, BDD	• sp^3 carbon • Low SA • High stability • Low conductivity • Doped • High resistance to poisoning	Pt (avg. 4.6 nm; 10–150 nm), Pt–Ru, Au, Pt–RuO_2, Pt–RuO_2–RhO_2, Pt–SnO_2 (avg. 5 nm) and Pt–Ta_2O_5 (avg. 9.1 nm)	–	–	Cathode	• Low metal stability and dispersion hence agglomeration and large NP size variation	[122] [123] [124] [125]
Graphene, FLG	• sp^2 carbon, rippled sheet structure • Hydrophobic • High conductivity • 10^3–10^4 S cm^{-1} • N-doping for ORR	Pt, Pd, Pt–Ru, Pt–Pd	44.6–81.6	390–440 (cathode)	Anode, cathode	• Often produced from reduced GO • Can also be prepared as vertically aligned 1–3 layers graphene (FLG) • High resistance to CO-poisoning • Properties depend on synthesis method used	[130] [131] [133] [136] [141] [237–239]
GO/RGO	• sp^2/sp^3 carbon • Variable conductivity • ≤10^4 S cm^{-1} • Hydrophilic • O-functional groups	Pt (2–6–nm), Pt–Ru	≤113	128	Anode	• O-defects promote uniform dispersal of NPs • Allows high loading with small particle size • O-species appear to increase CO-tolerance	[142] [146] [141] [145] [240]

shown in Fig. 15). Pt nanoparticles were then electrochemically deposited on PTy to obtain the Pt–PTy composite. The method allowed Pt loadings as low as 0.12 mg cm^{-2}. Electrochemical studies revealed high electrochemical active area and more efficient electrocatalyst utilisation. EIS and chronoamperometry studies showed that Pt on PTy exhibited slightly higher tolerance to CO poisoning and was less susceptible to deactivation which was attributed to the presence of large amount of Pt–OH species on the composite surface. However, it was also reported that the presence of PTy intermediary layer leads to partial deactivation of Pt nanoparticles [216]. Maiyalagan et al. used a PEDOT-V_2O_5 composite to support Pt nanoparticles and compared its performance with Pt/C towards MOR. TEM images showed porous morphology of PEDOT–V_2O_5 which favours methanol diffusion and also enabled good dispersion of Pt nanoparticles on the nanocomposite surface (average particle size: 2.3 nm). The Pt/PEDOT–V_2O_5 catalyst was reported to display interesting properties like (i) the presence of vanadium atom(s) encouraged several catalytic and electrocatalytic processes and (ii) the vanadium oxide (VO^{2+}/V^{3+}) redox couple favoured the oxidation of methanol [219].

Conducting polymers have the potential to be developed as ideal catalyst support in PEMFC and DMFC as they are gas and water permeable, and conduct protons as well as electrons. However, further development is still required for these to be successfully used as catalyst supports in commercial PEMFC and DMFC.

5. Hybrid supports

Pt, Pd and Pt–Ru and various other electrocatalysts supported on hybrid support systems consisting of a combination of both carbon and non-carbon support materials have also been extensively researched and developed [178,199,220–222]. Such an arrangement consists of a primary and a secondary support. For example, SnO_2 nanowires are often grown as secondary support on carbon fibres of carbon paper and platinum or other precious metal nanoparticle catalysts are deposited onto these nanowires [221,223].

Recently, Kou et al. produced and investigated Pt supported on ITO–graphene support [222]. The authors synthesised ITO nanocrystals directly on functionalized graphene sheets, forming an ITO-graphene hybrid. Pt nanoparticles are then deposited,

Table 2
Types of non-carbonaceous support materials: properties, catalysts and observations.

Type of support	Support properties	Catalysts (particle size); loading	ECSA ($m^2\ g^{-1}$)	Power density ($mW\ cm^{-2}$)	Electrode	Observations/comments	Ref.
TiO_{2-x} or Ti_nO_{2n-1}	• Semiconductor/conductor/proton conductor • Low SA, highly durable	Pt, Pd, PANI–Fe	233	560–1000 (cathode)	Anode, cathode	• Upto 10-fold higher ORR wrt Pt/C • Nb/Ru doping increases conductivity ($1.11\ S\ cm^{-1}$)	[153] [37] [154] [162]
TiN	• High electrical conductivity • $4000\ S\ cm^{-1}$ • Resistant to CO poisoning	Pt (3.2–20 nm) $0.022–0.03\ mg\ cm^{-2}$	70	–	Anode, cathode	• Low rate of corrosion under fuel cell conditions • Electrically passive in sulfuric acid media at temperatures >60 °C, due to the formation of –OH groups on surface	[38] [157] [241]
TiB_2	• Good conductivity • Excellent thermal stability • Corrosion resistance in acid medium	Pt 3.4 nm	34.7	–	Cathode	• High electrochemical stability	[158] [159]
ITO	• Semiconductor • $1000\ S\ cm^{-1}$ • High oxidation resistance	Pt (5–30 nm), Au (30 nm), Au–Pt (60 nm)	–	–	Anode, cathode	• Faster electron kinetics or lower charge transfer resistance • Agglomeration	[172] [173] [175] [42]
SiO_2	• Semiconductor • High oxidation resistance	Pt, Pt–Ru 2.2 nm	32–89.6	≤90	Anode, cathode	• Significantly reduced methanol crossover and control fuel feeding • Long-term durability in high methanol conc. • High mass activity	[43] [178] [179]
WO NPs, microspheres and NWs	• Semiconductor/proton conductor • $2.58\ S\ cm^{-1}$ • Low surface area • CO tolerant	Pt (1–3 nm) $0.18\ mg\ cm^{-2}$ Pt–Ru	63.5	–	Anode, cathode	• Forms tungsten trioxide hydrates to enable enhanced proton transfer	[181] [184] [185] [195] [49]
WC NPs, NWs, nanofibers, mesoporous	• Catalytic properties like Pt, synergistic effects • CO tolerant	Pt, Au, Pd, Ag	182	~200 (cathode)	Anode, cathode	• Crystallinity and pore structure of WC are affected by the temp. for the carburization • WC not stable at oxidation voltages above 0.8 V • Stability of WC can be improved by the presence of submonolayer coverages of Pt	[199] [200] [242] [50] [46]
SZ	• Proton conductor • Highly hydrophilic • $10^{-2}\ S\ m^{-1}$	Pt ~8 nm	80	–	Cathode	• Better than Pt/C in absence of Nafion • 50–100 nm SZ particles • High stability in fuel cell conditions	[51]
SnO_2 NPs, NWs	• High corrosion resistance • $10\ S\ cm^{-1}$	Pt 2–6 nm ≤50 wt.%	–	≤740 (cathode)	Anode, cathode	• Oxidation resistant • High tolerance to voltage cycling • High stability in fuel cell conditions • Sb doping improves corrosion resistance and electrochemical stability	[41] [163] [164]

on the ITO–graphene support using the polyol reduction process. This resulted in the formation of a unique triple-junction structure (Pt–ITO–graphene). Their experimental work was supported by DFT calculations and showed that the supported Pt nanoparticles are more stable at the Pt–ITO–graphene triple junctions. The DFT calculations further suggested that the defects and functional groups on graphene also played an important role in stabilizing the catalysts. While the graphene sheets provided a high surface are and high electrical conductivity; the evenly dispersed ITO nanoparticles were found to protect graphene against corrosion thereby protecting and enhancing the durability of the support. The electrochemical performance of the hybrid system was found to be much better compared to that of Pt–graphene. In another study, Wang et al. studied $Pt/CN_x/SiO_2$ catalyst–support system [178]. This study has already been described in an earlier section on SiO_2 supports. Both these systems showed higher electrocatalytic activity and

stability towards the ORR compared to Pt supported on Vulcan XC-72 [222,178]. Arbizzani et al. synthesised N-doped graphene and CNT on the mesopores of Xerogel carbon as ORR catalyst. The mesopores acted as a template for the growth of CNT and graphene structures. The authors observed the catalytic activity of the hybrid N-doped material for ORR in PEMFC conditions. It was found that the process required further work to increase concentration of the active sites as well as an optimization of the latter meso-macroporosity in order to enhance the contact between the catalytic layer and Nafion® [224]. Wu et al. have reported the fabrication and use of nitrogen doped onion like carbon material as support for Pt and Co–Fe and other non-precious metal nanoparticles for the ORR. The onion-like graphitic carbon material (N–Me–C) was synthesized by pyrolyzing a hexamethylene diamine–Me (Me:Co and Fe) complex. N–Me–C effectively catalysed ORR which was evidenced by RDE/RRDE data showing significant positive shifts of onset and half-wave ($E_{1/2}$) potentials and a drop in the H_2O_2 yield compared to traditional carbon supports [225,226].

The use of tungsten oxides and carbides with carbon nanostructures as primary as well as secondary supports has also attracted attention [195,227,228]. Ando et al. reported ammonia-treated carbon-supported cobalt tungsten as fuel cell cathode catalyst [229]. Nie et al. studied nanocrystalline WC supported Au–Pd catalyst for ORR [199]. The electrocatalysts were prepared using an intermittent microwave heating method. These studies showed promising results and potential for outperforming existing Pt-based electrocatalysts.

Guo et al. have investigated the use of different secondary supports like fluorine-SnO_2, sulphated TiO_2 and SZ with CNT as primary support in an attempt to explore novel hybrid supports for enhanced Pt performance in DMFCs [52,220,223]. Kakaroti et al. used a mixed oxide system of ceria and titania as support for 2–5 nm Pt nanoparticles to study the effect of synthesis technique on the catalytic activity of Pt [53].

6. Conclusions

Electrocatalyst supports play a vital role in asertaining the performance, durability and cost of PEMFC and DMFC systems. A myriad of nanostructured materials including carbon nanostuctures, metal oxides, conducting polymers and many hybrid conjugates have been exhaustively researched over the past few decades to improve the existing and also develop novel PEMFC/DMFC catalyst support. This article has reviewed the recent developments and investigations reported on various catalyst supports. Tables 1 and 2 summarize the cabonaceous and non-carbonaceous materials discussed in this review.

Many developments and inprovements can be seen in the structure, poisoning tolerance and stability of various nanostructured carbonaceous supports over the recent years. Consequently, these are now much more sturdy as cathode and anode support materials. New materials like graphene are also offering new avenues for research. Nevertheless, various degrees of carbon corrosion still persists for oxidised (and/or functionalised) carbonaceous supports. On the other hand, new structures, synthesis and surface modification techniques [30,31,78,79,98,115] suggest possibilities of further improvement; not only in corrosion resistance but also improved water handling capabilities whilst still maintaining good conductivity. Metal oxides and carbides (especially W and Ti) based nanostructures have shown interesting results with noble as well as non-precious metal electrocatalysts and have strong potential for furter development. The use of conducting polymers as supports has recently picked up pace. These possess promising capabilities for future developments. Considering their capability of proton and electron conductivity, water and gas permeability, these may even come to forefront as ideal supports in the near future. The use of hybrid supports can bring the best of both carbonaceous and non-carbonaceous supports. With dynamic research on various types of support, hybrids using conducting membranes with nanostructured carbon or metal oxides could certainly bring about a path-breaking change in PEMFC/DMFC catalyst–support systems.

An amalgamation of these novel electrocatalyst supports and improved catalyst loading techniques could bring about revolutionary changes in the quest for high performance, long-lasting PEMFC/DMFCs. However, more detailed investigations (MEA studies, continuous cycling and accelerated degradation tests) are still required to understand the behaviour of these materials under 'real' fuel cell conditions.

Acknowledgement

The authors would like to thank Dr. Navneet Soin at NIBEC, University of Ulster for his valuable discussions and inputs.

References

[1] N. Rajalakshmi, N. Lakshmi, K.S. Dhathathreyan, Int. J. Hydrogen Energy 33 (2008) 7521–7526.
[2] H.P. Bennetto, J.L. Stirling, K. Tanaka, C.A. Vega, Biotechnol. Bioeng. 25 (1983) 559–568.
[3] E. Ticianelli, C. Derouin, A. Redondo, S. Srinivasan, J. Electrochem. Soc. 135 (1988) 2209.
[4] O. Yamamoto, Y. Takeda, R. Kanno, M. Noda, Solid State Ionics 22 (1987) 241–246.
[5] K.S. Howe, K. Kendall, J. Fuel Cell Sci. Technol. 8 (2011) 034502.
[6] N. Sammes, Fuel Cell Technology: Reaching Towards Commercialization, Springer, London, 2006.
[7] L.J.M.J. Blomen, M.N. Mugerwa, Fuel Cell Systems, Plenum Press, New York, 1993.
[8] M.M. Mench, Fuel Cell Engines, John Wiley and Sons Ltd., London, 2008.
[9] G.D.J. Harper, Fuel Cell Projects for the Evil Genius, 2008.
[10] S. Srinivasan, Fuel Cells: From Fundamentals to Applications, Springer Verlag, 2006.
[11] A. Hermann, T. Chaudhuri, P. Spagnol, Int. J. Hydrogen Energy 30 (2005) 1297–1302.
[12] S. Cleghorn, X. Ren, T. Springer, M. Wilson, C. Zawodzinski, T. Zawodzinski, et al., Int. J. Hydrogen Energy 22 (1997) 1137–1144.
[13] S. Wasmus, A. Kuver, J. Electroanal. Chem. 461 (1999) 14–31.
[14] H. Uchida, Y. Mizuno, M. Watanabe, J. Electrochem. Soc. 149 (2002) A682.
[15] A.H.C. Sirk, J.M. Hill, S.K.Y. Kung, V.I. Birss, J. Phys. Chem. B. 108 (2004) 689–695.
[16] O.J. Curnick, P.M. Mendes, B.G. Pollet, Electrochem. Commun. 12 (2010) 1017–1020.
[17] S. Du, J. Power Sources 195 (2010) 289–292.
[18] P. Agnolucci, Int. J. Hydrogen Energy 32 (2007) 4319–4328.
[19] J. Andújar, F. Segura, Renew. Sustain. Energy Rev. 13 (2009) 2309–2322.
[20] M.T. Gencoglu, Z. Ural, Int. J. Hydrogen Energy 34 (2009) 5242–5248.
[21] Y. Lin, X. Cui, C. Yen, C.M. Wai, J. Phys. Chem. B: Conden. Phase 109 (2005) 14410–14415.
[22] A. Halder, S. Sharma, M.S. Hegde, N. Ravishankar, J. Phys. Chem. C 113 (2009) 1466–1473.
[23] J. Kua, W.A. Goddard III, J. Am. Chem. Soc. 121 (1999) 10928–10941.
[24] J. Chen, M. Wang, B. Liu, Z. Fan, K. Cui, Y. Kuang, J. Phys. Chem. B 110 (2006) 11775–11779.
[25] N. Jha, A. Leela Mohana Reddy, M.M. Shaijumon, N. Rajalakshmi, S. Ramaprabhu, Int. J. Hydrogen Energy 33 (2008) 427–433.
[26] C.J. Yang, Energy Policy 37 (2009) 1805–1808.
[27] Z. Liu, X. Lin, J.Y. Lee, W. Zhang, M. Han, L.M. Gan, Langmuir 18 (2002) 4054–4060.
[28] C. Wang, M. Waje, X. Wang, J.M. Tang, R.C. Haddon, Y. Yan, Nano Lett. 4 (2004) 345–348.
[29] C.H. Wang, H.Y. Du, Y.T. Tsai, C.P. Chen, C.J. Huang, L.C. Chen, et al., J. Power Sources 171 (2007) 55–62.
[30] Y.L. Hsin, K.C. Hwang, C.T. Yeh, J. Am. Chem. Soc. 129 (2007) 9999–10010.
[31] T. Maiyalagan, J. Solid State Electrochem. 13 (2009) 1561–1566.
[32] S. Song, Y. Liang, Z. Li, Y. Wang, R. Fu, D. Wu, et al., Appl. Catal. B: Environ. 98 (2010) 132–137.
[33] K. Honda, M. Yoshimura, T.N. Rao, D. Tryk, A. Fujishima, K. Yasui, et al., J. Electroanal. Chem. 514 (2001) 35–50.
[34] F. Montilla, E. Morallon, I. Duo, C. Comninellis, J.L. Vazquez, Electrochim. Acta 48 (2003) 3891–3897.
[35] (a) N. Spătaru, X. Zhang, T. Spătaru, D.A. Tryk, A. Fujishima, J. Electrochem. Soc. 155 (2008) B264–B269;

(b) E. Antolini, Appl. Catal. B: Environ. 88 (2009) 1–24;
(c) H. Liu, C. Song, L. Zhang, J. Zhang, H. Wang, D.P. Wilkinson, J. Power Sources 155 (2006) 95–110.
[36] E. Antolini, E.R. Gonzalez, Solid State Ionics 180 (2009) 746–763.
[37] M. Wang, D. Guo, H. Li, J. Solid State Chem. 178 (2005) 1996–2000.
[38] O.T.M. Musthafa, S. Sampath, Chem. Commun. (2008) 67–69.
[39] O.E. Haas, S.T. Briskeby, O.E. Kongstein, M. Tsypkin, R. Tunold, B.T. Borresen, Synthesis, J. New Mater. Electrochem. Syst. 11 (2008) 9–14.
[40] A. Wang, H. Xu, Y. Lu, J. Hu, X. Kong, B. Tian, et al., Chin. J. Catal. 30 (2009) 179–181.
[41] T. Okanishi, T. Matsui, T. Takeguchi, R. Kikuchi, K. Eguchi, Appl. Catal. A: Gen. 298 (2006) 181–187.
[42] H. Chhina, S. Campbell, O. Kesler, J. Power Sources 161 (2006) 893–900.
[43] B. Seger, A. Kongkanand, K. Vinodgopal, P.V. Kamat, J. Electroanal. Chem. 621 (2008) 198–204.
[44] P.J. Kulesza, L.R. Faulkner, Electrodeposition, J. Electrochem. Soc. 136 (1989) 707–713.
[45] P.J. Kulesza, L.R. Faulkner, J. Electroanal. Chem. Interfacial Electrochem. 259 (1989) 81–98.
[46] E.C. Weigert, A.L. Stottlemyer, M.B. Zellner, J.G. Chen, J. Phys. Chem. C 111 (2007) 14617–14620.
[47] J.P. Bosco, K. Sasaki, M. Sadakane, W. Ueda, J.G. Chen, Synthesis, Chem. Mater. 22 (2010) 966–973.
[48] T. Oh, J.Y. Kim, Y. Shin, M. Engelhard, K.S. Weil, J. Power Sources 196 (2011) 6099–6103.
[49] R. Ganesan, J.S. Lee, J. Power Sources 157 (2006) 217–221.
[50] G. Cui, P.K. Shen, H. Meng, J. Zhao, G. Wu, J. Power Sources 196 (2011) 6125–6130.
[51] Y. Suzuki, A. Ishihara, S. Mitsushima, N. Kamiya, K. Ota, Electrochem. Solid-State Lett. 10 (2007) B105–B107.
[52] D.J. Guo, X.P. Qiu, W.T. Zhu, L.Q. Chen, Appl. Catal. B: Environ. 89 (2009) 597–601.
[53] A.S. Karakoti, J.E.S. King, A. Vincent, S. Seal, Appl. Catal. A: Gen. 388 (2010) 262–271.
[54] G. Che, B.B. Lakshmi, E.R. Fisher, C.R. Martin, Nature 393 (1998) 346–349.
[55] D.B. Mawhinney, V. Naumenko, A. Kuznetsova, J.T. Yates Jr., J. Liu, R. Smalley, J. Am. Chem. Soc. 122 (2000) 2383–2384.
[56] W. Jeffrey, R.M. Stroud, K.E. Swider-Lyons, D.R. Rolison, J. Phys. Chem. B 104 (2000) 9772–9776.
[57] P.V. Dudin, P.R. Unwin, J.V. Macpherson, J. Phys. Chem. C 114 (2010) 13241–13248.
[58] T. Matsumoto, T. Komatsu, K. Arai, T. Yamazaki, M. Kijima, H. Shimizu, et al., Chem. Commun. (2004) 840–841.
[59] X. Li, I. Hsing, Electrochim. Acta 51 (2006) 5250–5258.
[60] V. Baglio, A. Di Blasi, C. D'Urso, V. Antonucci, A. Aricò, R. Ornelas, et al., J. Electrochem. Soc. 155 (2008) B829.
[61] D. Nagao, Y. Shimazaki, S. Saeki, Y. Kobayashi, M. Konno, Colloids Surf. Physicochem. Eng. Aspects 302 (2007) 623–627.
[62] C. Yang, X. Hu, D. Wang, C. Dai, L. Zhang, H. Jin, et al., J. Power Sources 160 (2006) 187–193.
[63] K.T. Jeng, C.C. Chien, N.Y. Hsu, S.C. Yen, S.D. Chiou, S.H. Lin, et al., J. Power Sources 160 (2006) 97–104.
[64] S.L. Knupp, W. Li, O. Paschos, T.M. Murray, J. Snyder, P. Haldar, Carbon 46 (2008) 1276–1284.
[65] Z. Liu, J.Y. Lee, W. Chen, M. Han, L.M. Gan, Langmuir 20 (2004) 181–187.
[66] R. Zacharia, S. Rather, S.W. Hwang, K.S. Nahm, Chem. Phys. Lett. 434 (2007) 286–291.
[67] N. Soin, S. Roy, L. Karlsson, J. McLaughlin, Diamond Related Mater. 19 (2010) 595–598.
[68] B. Satishkumar, E.M. Vogl, A. Govindaraj, C. Rao, J. Phys. D 29 (1996) 3173.
[69] A. Guha, W. Lu, T.A. Zawodzinski Jr., D.A. Schiraldi, Carbon 45 (2007) 1506–1517.
[70] K. Yasuda, Y. Nishimura, Mater. Chem. Phys. 82 (2003) 921–928.
[71] Y. Shao, G. Yin, J. Wang, Y. Gao, P. Shi, J. Power Sources 161 (2006) 47–53.
[72] T.M. Day, P.R. Unwin, J.V. Macpherson, Nano Lett. 7 (2007) 51–57.
[73] T.M. Day, P.R. Unwin, N.R. Wilson, J.V. Macpherson, J. Am. Chem. Soc. 127 (2005) 10639–10647.
[74] T.W. Ebbesen, H. Hiura, M.E. Bisher, M.M.J. Treacy, J.L. Shreeve-Keyer, R.C. Haushalter, Adv. Mater. 8 (1996) 155–157.
[75] L. Gan, R. Lv, H. Du, B. Li, F. Kang, Electrochem. Commun. 11 (2009) 355–358.
[76] Z. Tang, C.K. Poh, K.K. Lee, Z. Tian, D.H.C. Chua, J. Lin, J. Power Sources 195 (2010) 155–159.
[77] (a) C.T. Hsieh, J.L. Wei, J.Y. Lin, B.H. Yang, Diamond Related Mater. (2011);
(b) E. Antolini, Appl. Catal. B: Environ. 74 (2007) 337–350.
[78] R. Ahmadi, M.K. Amini, Int. J. Hydrogen Energy 36 (2011) 7275–7283.
[79] S. Park, Y. Shao, R. Kou, V.V. Viswanathan, S.A. Towne, P.C. Rieke, et al., J. Electrochem. Soc. 158 (2011) B297–B302.
[80] D. He, C. Zeng, C. Xu, N. Cheng, H. Li, S. Mu, et al., Langmuir 27 (2011) 5582–5588.
[81] H.S. Oh, K. Kim, H. Kim, Int. J. Hydrogen Energy (2011).
[82] B. Wu, D. Hu, Y. Kuang, Y. Yu, X. Zhang, J. Chen, Chem. Commun. (2011).
[83] Y. Zhao, X. Yang, J. Tian, F. Wang, L. Zhan, J. Power Sources 195 (2010) 4634–4640.
[84] M.W. Xu, Z. Su, Z.W. Weng, Z.C. Wang, B. Dong, Mater. Chem. Phys. (2010).
[85] K. Gong, F. Du, Z. Xia, M. Durstock, L. Dai, Science 323 (2009) 760–763.
[86] Z. Chen, D. Higgins, H. Tao, R.S. Hsu, Z. Chen, J. Phys. Chem. C 113 (2009) 21008–21013.
[87] D. Yu, Q. Zhang, L. Dai, J. Am. Chem. Soc. (2010).
[88] Y. Tang, B.L. Allen, D.R. Kauffman, A. Star, J. Am. Chem. Soc. 131 (2009) 13200–13201.
[89] S. Ghosh, C.R. Raj, J. Phys. Chem. C 114 (2010) 10843–10849.
[90] N.M. Rodriguez, M.S. Kim, R.T.K. Baker, J. Phys. Chem. 98 (1994) 13108–13111.
[91] Z. Lin, L. Ji, W.E. Krause, X. Zhang, J. Power Sources 195 (2010) 5520–5526.
[92] J.S. Zheng, X.S. Zhang, P. Li, J. Zhu, X.G. Zhou, W.K. Yuan, Electrochem. Commun. 9 (2007) 895–900.
[93] W. Li, M. Waje, Z. Chen, P. Larsen, Y. Yan, Carbon 48 (2010) 995–1003.
[94] S. Kang, S. Lim, D.H. Peck, S.K. Kim, D.H. Jung, S.H. Hong, et al., Int. J. Hydrogen Energy (2011).
[95] J.S. Zheng, X.S. Zhang, P. Li, X.G. Zhou, W.K. Yuan, Catal. Today 131 (2008) 270–277.
[96] J.S. Zheng, M.X. Wang, X.S. Zhang, Y.X. Wu, P. Li, X.G. Zhou, et al., J. Power Sources 175 (2008) 211–216.
[97] D. Sebastián, M. Lázaro, I. Suelves, R. Moliner, V. Baglio, A. Stassi, et al., Int. J. Hydrogen Energy (2011).
[98] L. Zhang, C. Zhang, X. Xiang, F. Li, Chem. Eng. Technol. 33 (2010) 44–51.
[99] R. Ryoo, S.H. Joo, S. Jun, J. Phys. Chem. B 103 (1999) 7743–7746.
[100] R. Ryoo, S.H. Joo, M. Kruk, M. Jaroniec, Adv. Mater. 13 (2001) 677–681.
[101] J. Ding, K.Y. Chan, J. Ren, F. Xiao, Electrochim. Acta 50 (2005) 3131–3141.
[102] F. Su, J. Zeng, X. Bao, Y. Yu, J.Y. Lee, X.S. Zhao, Chem. Mater. 17 (2005) 3960–3967.
[103] S.H. Joo, C. Pak, D.J. You, S.A. Lee, H.I. Lee, J.M. Kim, et al., Electrochim. Acta 52 (2006) 1618–1626.
[104] H. Chang, S.H. Joo, C. Pak, J. Mater. Chem. 17 (2007) 3078–3088.
[105] G. Zhao, J. He, C. Zhang, J. Zhou, X. Chen, T. Wang, J. Phys. Chem. C 112 (2008) 1028–1033.
[106] J.R.C. Salgado, F. Alcaide, G. Álvarez, L. Calvillo, M.J. Lázaro, E. Pastor, J. Power Sources 195 (2010) 4022–4029.
[107] B. Liu, S. Creager, Electrochim. Acta 55 (2010) 2721–2726.
[108] L. Calvillo, M. Gangeri, S. Perathoner, G. Centi, R. Moliner, M.J. Lázaro, Int. J. Hydrogen Energy 36 (2011) 9805–9814.
[109] S. Hwang, G.G. Park, S.D. Yim, S.H. Park, T.H. Yang, H. Kim, et al., Curr. Appl. Phys. 10 (2010) S69–S72.
[110] M.L. Lin, M.Y. Lo, C.Y. Mou, J. Phys. Chem. C 113 (2009) 16158–16168.
[111] X. Cui, J. Shi, L. Zhang, M. Ruan, J. Gao, Carbon 47 (2009) 186–194.
[112] S.H. Joo, H.I. Lee, D.J. You, K. Kwon, J.H. Kim, Y.S. Choi, et al., Carbon 46 (2008) 2034–2045.
[113] S.H. Liu, J.R. Wu, Int. J. Hydrogen Energy (2010).
[114] R. Liu, D. Wu, X. Feng, K. Müllen, Angew. Chem. Int. Ed. 49 (2010) 2565–2569.
[115] G.M. Swain, Adv. Mater. 6 (1994) 388–392.
[116] J. Xu, M.C. Granger, Q. Chen, J.W. Strojek, T.E. Lister, G.M. Swain, Anal. Chem. 69 (1997) 591–597.
[117] Q. Chen, M.C. Granger, T.E. Lister, G.M. Swain, J. Electrochem. Soc. 144 (1997) 3806.
[118] J. Wang, J.H. Andreasen, B. Karihaloo, Composites Sci. Technol. 60 (2000) 75–82.
[119] T.A. Ivandini, R. Sato, Y. Makide, A. Fujishima, Y. Einaga, Diamond Related Mater. 14 (2005) 2133–2138.
[120] J.A. Bennett, Y. Show, S. Wang, G.M. Swain, J. Electrochem. Soc. 152 (2005) E184.
[121] J. Hu, X. Lu, J.S. Foord, Q. Wang, Phys. Stat. Sol. (a) 206 (2009) 2057–2062.
[122] G.R. Salazar-Banda, H.B. Suffredini, M.L. Calegaro, S.T. Tanimoto, L.A. Avaca, J. Power Sources 162 (2006) 9–20.
[123] G.R. Salazar-Banda, K.I.B. Eguiluz, L.A. Avaca, Electrochem. Commun. 9 (2007) 59–64.
[124] G.R. Salazar-Banda, H.B. Suffredini, L.A. Avaca, S.A.S. Machado, Mater. Chem. Phys. 117 (2009) 434–442.
[125] X. Lu, J. Hu, J.S. Foord, Q. Wang, J. Electroanal. Chem. 654 (2011) 38–43.
[126] L. La-Torre-Riveros, K. Soto, M.A. Scibioh, C.R. Cabrera, J. Electrochem. Soc. 157 (2010) B831.
[127] A. Moore, V. Celorrio, M.M. de Oca, D. Plana, W. Hongthani, M.J. Lázaro, et al., Chem. Commun. (2011).
[128] K.S. Novoselov, A.K. Geim, S.V. Morozov, D. Jiang, M.I.K.I.V. Grigorieva, S.V. Dubonos, et al., Nature 438 (2005) 197–200.
[129] Y.C. Cao, C. Xu, X. Wu, X. Wang, L. Xing, K. Scott, J. Power Sources (2011).
[130] S. Liu, J. Wang, J. Zeng, J. Ou, Z. Li, X. Liu, et al., J. Power Sources 195 (2010) 4628–4633.
[131] L. Qu, Y. Liu, J.B. Baek, L. Dai, ACS Nano 4 (2010) 1321–1326.
[132] N. Soin, S.S. Roy, T.H. Lim, J.A.D. McLaughlin, Mater. Chem. Phys. 129 (2011) 1051–1057.
[133] S. Guo, S. Dong, E. Wang, ACS Nano 4 (2009) 547–555.
[134] S. Sirč, C. Crisafulli, S. Giuffrida, G. Ventimiglia, C. Bongiorno, C. Spinella, J. Mol. Catal. A: Chem. 333 (2010) 100–108.
[135] N. Jha, R.I. Jafri, N. Rajalakshmi, S. Ramaprabhu, Int. J. Hydrogen Energy 36 (2011) 7284–7290.
[136] R.I. Jafri, N. Rajalakshmi, S. Ramaprabhu, J. Mater. Chem. 20 (2010) 7114–7117.
[137] D.A. Dikin, S. Stankovich, E.J. Zimney, R.D. Piner, G.H.B. Dommett, G. Evmenenko, et al., Nature 448 (2007) 457–460.
[138] C. Gómez-Navarro, R.T. Weitz, A.M. Bittner, M. Scolari, A. Mews, M. Burghard, et al., Nano Lett. 7 (2007) 3499–3503.
[139] G. Eda, G. Fanchini, M. Chhowalla, Nature 3 (2008) 270–274.

[140] G. Williams, B. Seger, P.V. Kamat, ACS Nano 2 (2008) 1487–1491.
[141] Y. Li, W. Gao, L. Ci, C. Wang, P.M. Ajayan, Carbon 48 (2009) 1124–1130.
[142] S. Sharma, A. Ganguly, P. Papakonstantinou, X. Miao, M. Li, J.L. Hutchison, et al., J. Phys. Chem. C 114 (2010) 19459–19466.
[143] S. Wang, S.P. Jiang, X. Wang, Electrochim. Acta 56 (2011) 3338–3344.
[144] J. Qiu, G.C. Wang, R. Liang, X.H. Xia, H.W. Yu, J. Phys. Chem. C 115 (2011) 15639–15645.
[145] H.W. Ha, I.Y. Kim, S.J. Hwang, R.S. Ruoff, Electrochem. Solid-State Lett. 14 (2011) B70–B73.
[146] X. Chen, G. Wu, J. Chen, X. Chen, Z. Xie, X. Wang, J. Am. Chem. Soc. 133 (2011) 3693–3695.
[147] S. Maass, F. Finsterwalder, G. Frank, R. Hartmann, C. Merten, J. Power Sources 176 (2008) 444–451.
[148] Y. Fovet, J.Y. Gal, F. Toumelin-Chemla, Talanta 53 (2001) 1053–1063.
[149] F. Leroux, P.J. Dewar, M. Intissar, G. Ouvrard, L.F. Nazar, J. Mater. Chem. 12 (2002) 3245–3253.
[150] B.E. Hayden, D.V. Malevich, D. Pletcher, Electrochem. Commun. 3 (2001) 390–394.
[151] G. Chen, S.R. Bare, T.E. Mallouk, J. Electrochem. Soc. 149 (2002) A1092–A1099.
[152] D.S. Kim, E.F.A. Zeid, Y.T. Kim, Electrochim. Acta 55 (2010) 3628–3633.
[153] S.Y. Huang, P. Ganesan, B.N. Popov, Appl. Catal. B: Environ. 102 (2011) 71–77.
[154] G. Wu, M.A. Nelson, N.H. Mack, S. Ma, P. Sekhar, F.H. Garzon, et al., Chem. Commun. 46 (2010) 7489–7491.
[155] I. Milošv, H.H. Strehblow, B. Navinšek, M. Metikoš-Huković, Surf. Interface Anal. 23 (1995) 529–539.
[156] S.T. Oyama, The Chemistry of Transition Metal Carbides and Nitrides, Kluwer Academic Publishers, 1996.
[157] B. Avasarala, P. Haldar, Int. J. Hydrogen Energy 36 (2011) 3965–3974.
[158] B. Basu, G.B. Raju, A.K. Suri, Int. Mater. Rev. 51 (2006) 352–374.
[159] S. Yin, S. Mu, H. Lv, N. Cheng, M. Pan, Z. Fu, Appl. Catal. B: Environ. 93 (2010) 233–240.
[160] D. Morris, Y. Dou, J. Rebane, C.E.J. Mitchell, R.G. Egdell, D.S.L. Law, et al., Phys. Rev. B 61 (2000) 13445–13457.
[161] H. Chhina, S. Campbell, O. Kesler, J. Electrochem. Soc. 156 (2009) B1232.
[162] S.Y. Huang, P. Ganesan, B.N. Popov, Appl. Catal. B: Environ. 96 (2010) 224–231.
[163] A. Masao, S. Noda, F. Takasaki, K. Ito, K. Sasaki, Electrochem. Solid-State Lett. 12 (2009) B119–B122.
[164] P. Zhang, S.Y. Huang, B.N. Popov, J. Electrochem. Soc. 157 (2010) B1163–B1172.
[165] M. Nakada, A. Ishihara, S. Mitsushima, N. Kamiya, K. Ota, Electrochem. Solid-State Lett. 10 (2007) F1–F4.
[166] D.J. You, K. Kwon, C. Pak, H. Chang, Catal. Today 146 (2009) 15–19.
[167] K.S. Lee, I.S. Park, Y.H. Cho, D.S. Jung, N. Jung, H.Y. Park, et al., J. Catal. 258 (2008) 143–152.
[168] Y.S. Kim, H.S. Jang, W.B. Kim, J. Mater. Chem. 20 (2010) 7859–7863.
[169] H.L. Pang, X.H. Zhang, X.X. Zhong, B. Liu, X.G. Wei, Y.F. Kuang, et al., J. Colloid Interface Sci. 319 (2008) 193–198.
[170] J.C.C. Fan, J.B. Goodenough, J. Appl. Phys. 48 (1977) 3524–3531.
[171] (a) M. Yamaguchi, A. Ide-Ektessabi, H. Nomura, N. Yasui, Thin Solid Films 447 (2004) 115–118;
(b) Y. Shao, J. Liu, Y. Wang, Y. Lin, J. Mater. Chem. 19 (2008) 46–59.
[172] T. Minami, Thin Solid Films 516 (2008) 5822–5828.
[173] I.S. Park, E. Lee, A. Manthiram, J. Electrochem. Soc. 157 (2010) B251–B255.
[174] H. Zhang, W. Zhou, Y. Du, P. Yang, C. Wang, Electrochem. Commun. 12 (2010) 882–885.
[175] Y. Song, Y. Ma, Y. Wang, J. Di, Y. Tu, Electrochim. Acta 55 (2010) 4909–4914.
[176] X. Zhu, H. Zhang, Y. Zhang, Y. Liang, X. Wang, B. Yi, J. Phys. Chem. B 110 (2006) 14240–14248.
[177] L. Wang, D.M. Xing, Y.H. Liu, Y.H. Cai, Z.G. Shao, Y.F. Zhai, J. Power Sources 161 (2006) 61–67.
[178] R. Wang, X. Li, H. Li, Q. Wang, H. Wang, W. Wang, et al., Int. J. Hydrogen Energy 36 (2011) 5775–5781.
[179] K. Nam, S. Lim, S.K. Kim, S.H. Yoon, D.H. Jung, Int. J. Hydrogen Energy (2011).
[180] J.E. In, The Elements, Clarendon Press, Oxford, 1991.
[181] H. Chhina, S. Campbell, O. Kesler, J. Electrochem. Soc. 154 (2007) B533–B539.
[182] S.H. Lee, R. Deshpande, P.A. Parilla, K.M. Jones, B. To, A.H. Mahan, et al., Adv. Mater. 18 (2006) 763–766.
[183] L.W. Niedrach, H.I. Zeliger, J. Electrochem. Soc. 116 (1969) 152–153.
[184] Y.M. Li, M. Hibino, M. Miyayania, T. Kudo, Solid State Ionics 134 (2000) 271–279.
[185] H. Nakajima, I. Honma, Solid State Ionics 148 (2002) 607–610.
[186] E. Antolini, E.R. Gonzalez, Appl. Catal. B: Environ. 96 (2010) 245–266.
[187] P.K. Shen, A.C.C. Tseung, J. Electrochem. Soc. 141 (1994) 3082–3090.
[188] K.W. Park, K.S. Ahn, J.H. Choi, Y.C.a.K. Nah, Y.M. Li, Appl. Phys. Lett. 81 (2002) 907–909.
[189] K.W. Park, K.S. Ahn, Y.C. Nah, J.H. Choi, Y.E. Sung, J. Phys. Chem. B 107 (2003) 4352–4355.
[190] K.Y. Chen, P.K. Shen, A.C.C. Tseung, J. Electrochem. Soc. 142 (1995) L185–L187.
[191] Z. Sun, H.C.a.T. Chiu, A.C.C. Tseung, Electrochem. Solid-State Lett. 4 (2001) E9–E12.
[192] U.O. Kraovec, B. Orel, A. Georg, V. Wittwer, Solar Energy 68 (2000) 541–551.
[193] E.J. McLeod, V.I. Birss, Electrochim. Acta 51 (2005) 684–693.
[194] F. Micoud, F. Maillard, A. Bonnefont, N. Job, M. Chatenet, Phys. Chem. Chem. Phys. 12 (2009) 1182–1193.
[195] M.S. Saha, Y. Zhang, M. Cai, X. Sun, Int. J. Hydrogen Energy (2011).
[196] R.V. Sara, J. Am. Ceram. Soc. 48 (1965) 251–257.
[197] R.B. Levy, M. Boudart, Science 181 (1973) 547–549.
[198] M.B. Zellner, J.G. Chen, Catal. Today 99 (2005) 299–307.
[199] M. Nie, P.K. Shen, Z. Wei, J. Power Sources 167 (2007) 69–73.
[200] H. Meng, P.K. Shen, Electrochem. Commun. 8 (2006) 588–594.
[201] Z. Fu, Q. Huang, X. Xiang, Y. Lin, W. Wu, S. Hu, et al., Int. J. Hydrogen Energy (2011).
[202] X. Zhou, Y. Qiu, J. Yu, J. Yin, S. Gao, Int. J. Hydrogen Energy 36 (2011) 7398–7404.
[203] G.D. Yadav, J.J. Nair, Micropor. Mesopor. Mater. 33 (1999) 1–48.
[204] S. Hara, M. Miyayama, Solid State Ionics 168 (2004) 111–116.
[205] S. Tominaka, N. Akiyama, F. Croce, T. Momma, B. Scrosati, T. Osaka, J. Power Sources 185 (2008) 656–663.
[206] Z. Qi, Chem. Commun. (1998) 15–16.
[207] M. Lefebvre, Z. Qi, D. Rana, P.G. Pickup, Chem. Mater. 11 (1999) 262–268.
[208] C.W. Kuo, L.M. Huang, T.C. Wen, A. Gopalan, J. Power Sources 160 (2006) 65–72.
[209] K. Tintula, S. Pitchumani, P. Sridhar, A. Shukla, J. Chem. Sci. 122 (2010) 381–389.
[210] J.F. Drillet, R. Dittmeyer, K. Jüttner, L. Li, K.M. Mangold, Fuel Cells 6 (2006) 432–438.
[211] J.F. Drillet, R. Dittmeyer, K. Jüttner, J. Appl. Electrochem. 37 (2007) 1219–1226.
[212] J.H. Choi, K.W. Park, H.K. Lee, Y.M. Kim, J.S. Lee, Y.E. Sung, Electrochim. Acta 48 (2003) 2781–2789.
[213] J.H. Choi, Y.M. Kim, J.S. Lee, K.Y. Cho, H.Y. Jung, J.K. Park, et al., Solid State Ionics 176 (2005) 3031–3034.
[214] S.P. Jiang, Z. Liu, H.L. Tang, M. Pan, Electrochim. Acta 51 (2006) 5721–5730.
[215] C. Jiang, X. Lin, J. Power Sources 164 (2007) 49–55.
[216] T. Spătaru, M. Marcu, L. Preda, P. Osiceanu, J.M.C. Moreno, N. Spătaru, J. Solid State Chem. 15 (2011) 1149–1157.
[217] R. Lofrano, J. Madurro, J. Romero, J. Mol. Catal. A: Chem. 153 (2000) 237–242.
[218] R. Lofrano, J. Madurro, L. Abrantes, J. Romero, J. Mol. Catal. A: Chem. 218 (2004) 73–79.
[219] T. Maiyalagan, B. Viswanathan, Mater. Chem. Phys. 121 (2010) 165–171.
[220] D.J. Guo, X.P. Qiu, L.Q. Chen, W.T. Zhu, Carbon 47 (2009) 1680–1685.
[221] X. Zhang, H. Zhu, Z. Guo, Y. Wei, F. Wang, J. Power Sources 196 (2010) 3048–3053.
[222] R. Kou, Y. Shao, D. Mei, Z. Nie, D. Wang, C. Wang, et al., J. Am. Chem. Soc. 133 (2011) 2541–2547.
[223] D.J. Guo, Z.H. Jing, J. Colloid Interface Sci. 359 (2011) 257–260.
[224] C. Arbizzani, S. Righi, F. Soavi, M. Mastragostino, Int. J. Hydrogen Energy 36 (2011) 5038–5046.
[225] G. Wu, C. Dai, D. Wang, D. Li, N. Li, J. Mater. Chem. 20 (2010) 3059–3068.
[226] G. Wu, M. Nelson, S. Ma, H. Meng, G. Cui, P.K. Shen, Carbon 49 (2011) 3972–3982.
[227] Z. Zhao, X. Fang, Y. Li, Y. Wang, P.K. Shen, F. Xie, et al., Electrochem. Commun. 11 (2009) 290–293.
[228] M.S. Saha, M.N. Banis, Y. Zhang, R. Li, X. Sun, M. Cai, et al., J. Power Sources 192 (2009) 330–335.
[229] T. Ando, S. Izhar, H. Tominaga, M. Nagai, Electrochim. Acta 55 (2010) 2614–2621.
[230] C.T. Hsieh, J.Y. Lin, J.L. Wei, Int. J. Hydrogen Energy 34 (2009) 685–693.
[231] D. Sebastián, J. Calderón, J. González-Expósito, E. Pastor, M. Martínez-Huerta, I. Suelves, et al., Int. J. Hydrogen Energy 35 (2010) 9934–9942.
[232] L.B. Kong, H. Li, J. Zhang, Y.C. Luo, L. Kang, Appl. Surf. Sci. 256 (2010) 6688–6693.
[233] G. Liu, X. Li, P. Ganesan, B.N. Popov, Appl. Catal. B: Environ. 93 (2009) 156–165.
[234] E.P. Ambrosio, C. Francia, M. Manzoli, N. Penazzi, P. Spinelli, Int. J. Hydrogen Energy 33 (2008) 3142–3145.
[235] Z.P. Sun, X.G. Zhang, Y.Y. Liang, H. Tong, R.L. Xue, S.D. Yang, et al., J. Electroanal. Chem. 633 (2009) 1–6.
[236] K.K. Tintula, A.K. Sahu, A. Shahid, S. Pitchumani, P. Sridhar, A.K. Shukla, J. Electrochem. Soc. 157 (2010) B1679–B1685.
[237] L. Dong, R.R.S. Gari, Z. Li, M.M. Craig, S. Hou, Carbon 48 (2010) 781–787.
[238] S. Bong, Y.R. Kim, I. Kim, S. Woo, S. Uhm, J. Lee, et al., Electrochem. Commun. 12 (2009) 129–131.
[239] Y.H. Lu, M. Zhou, C. Zhang, Y.P. Feng, J. Phys. Chem. C 113 (2009) 20156–20160.
[240] S. Park, J. An, I. Jung, R.D. Piner, S.J. An, X. Li, et al., Nano Lett. 9 (2009) 1593–1597.
[241] K. Kakinuma, Y. Wakasugi, M. Uchida, T. Kamino, H. Uchida, M. Watanabe, Electrochem. Soc. (2010).
[242] H. Meng, P.K. Shen, Z. Wei, Electrochem. Solid-State Lett. 9 (2006) A368–A372.
[243] A.L. Dicks, J. Power Sources 156 (2006) 128–141.
[244] Y. Shao, G. Yin, J. Zhang, Y. Gao, Electrochim. Acta 51 (2006) 5853–5857.
[245] H.T. Fang, C.G. Liu, C. Liu, F. Li, M. Liu, H.M. Cheng, Chem. Mater. 16 (2004) 5744–5750.
[246] L. Li, Y. Xing, J. Electrochem. Soc. 153 (2006) A1823.
[247] B. Viswanathan, Catal. Today 141 (2009) 52–55.
[248] J. Wang, G. Yin, Y. Shao, Z. Wang, Y. Gao, J. Phys. Chem. C 112 (2008) 5784–5789.
[249] F. Coloma, A. Sepulveda-Escribano, J. Fierro, F. Rodriguez-Reinoso, Langmuir 10 (1994) 750–755.
[250] Z. Kowalczyk, J. Sentek, S. Jodzis, R. Diduszko, A. Presz, A. Terzyk, et al., Carbon 34 (1996) 403–409.
[251] M. Kang, M.W. Song, C.H. Lee, React. Kinet. Catal. Lett. 80 (2003) 131–138.
[252] M. Kang, Y.S. Bae, C.H. Lee, Carbon 43 (2005) 1512–1516.

[253] E.S. Steigerwalt, G.A. Deluga, D.E. Cliffel, C. Lukehart, J. Phys. Chem. B 105 (2001) 8097–8101.
[254] C.A. Bessel, K. Laubernds, N.M. Rodriguez, R.T.K. Baker, J. Phys. Chem. B 105 (2001) 1115–1118.
[255] X. Yu, S. Ye, J. Power Sources 172 (2007) 133–144.
[256] M. Kim, J.N. Park, H. Kim, S. Song, W.H. Lee, J. Power Sources 163 (2006) 93–97.
[257] A. Więckowski, E.R. Savinova, Catalysis and Electrocatalysis at Nanoparticle Surfaces, CRC, 2003.
[258] D.J. Suh, P. Tae-Jin, I. Son-Ki, Carbon 31 (1993) 427–435.
[259] N.H. Sagert, R.M.L. Pouteau, Platinum Met. Rev. 19 (1975) 16–21.
[260] X. Li, T. Radojicic, R. Vanselow, Surf. Sci. 225 (1990) L29–L32.
[261] K. Kwon, S. Jin, C. Pak, H. Chang, S.H. Joo, H.I. Lee, et al., Catal. Today 164 (2011) 186–189.
[262] E. Hegenberger, N. Wu, J. Phillips, J. Phys. Chem. 91 (1987) 5067–5071.
[263] C. Bittencourt, M. Hecq, A. Felten, J. Pireaux, J. Ghijsen, M. Felicissimo, et al., Chem. Phys. Lett. 462 (2008) 260–264.
[264] L. Calvillo, V. Celorrio, R. Moliner, M. Lázaro, Mater. Chem. Phys. 127 (2011) 335–341.
[265] P. Serp, M. Corrias, P. Kalck, Appl. Catal. A: Gen. 253 (2003) 337–358.
[266] J. Salgado, F. Alcaide, G. Álvarez, L. Calvillo, M. Lázaro, E. Pastor, J. Power Sources 195 (2010) 4022–4029.
[267] J. Chen, M.A. Hamon, H. Hu, Y. Chen, A.M. Rao, P.C. Eklund, et al., Science 282 (1998) 95.
[268] F. Ficicioglu, F. Kadirgan, J. Electroanal. Chem. 430 (1997) 179–182.
[269] Y. Zhou, B. He, W. Zhou, J. Huang, X. Li, B. Wu, et al., Electrochim. Acta 49 (2004) 257–262.
[270] G. Wu, Y.S. Chen, B.Q. Xu, Electrochem. Commun. 7 (2005) 1237–1243.
[271] Y. Zhang, M.L. Toebes, A. Van Der Eerden, W.E. O'Grady, K.P. De Jong, D.C. Koningsberger, J. Phys. Chem. B 108 (2004) 18509–18519.
[272] M.L. Toebes, Y. Zhang, J. Hájek, T. Alexander Nijhuis, J.H. Bitter, A. Jos van Dillen, et al., J. Catal. 226 (2004) 215–225.
[273] A. Lewera, L. Timpermen, A. Roguska, N. Alonso-Vante, J. Phys. Chem. C 115 (2011) 20153–20159.
[274] T. Matsui, T. Okanishi, K. Fujiwara, K. Tsutsui, R. Kikuchi, T. Takeguchi, et al., Sci. Technol. Adv. Mater. 7 (2006) 524–530.